# The Effects of Spatial Reconstruction and Flux Solver on the Performance of High-Order Finite-Volume Compressible Flow Solvers

Chengxiang Li<sup>1,5</sup>, Xing Ji<sup>2</sup>, Kun Xu<sup>1,3,4</sup> and Lian-Ping Wang<sup>5,\*</sup>

Received 2 August 2024; Accepted (in revised version) 17 May 2025

Abstract. Most high-order computational fluid dynamics methods for compressible flows are based on the Riemann solver for the flux evaluation and high-order interpolation or reconstruction such as the Weighted Essential Non-Oscillatory (WENO) scheme for spatial accuracy. The advantage of this kind of combination is the easy implementation and the ability to achieve the required spatial accuracy. However, despite the extensive research on high-order spatial reconstruction in the past, solvers coupling high-order space and time schemes have not been systematically evaluated. In this paper, based on the same fifth-order finite volume method (FVM), comparisons of the performance of the same flux solver with different reconstructions and the same reconstruction but different flux solvers are carried out on a structured mesh. For reconstruction, the TENO scheme and classic WENO-Z reconstruction have been chosen as representative methods. Meanwhile, for the flux solver, Lax-Friedrichs (LF) Riemann solver, HLLC solver, and GKS are considered. Through a series of simulated comparison cases, the unique characteristics of GKS and TENO have been demonstrated. Overall, the comparisons suggest that proper spatial and temporal coupling is important for accurate shock and vortex capturing.

AMS subject classifications: 76N17, 76M12, 35Q30, 35Q20

**Key words**: TENO reconstruction, Gas-kinetic scheme (GKS), Lax-Friedrichs Riemann solver, high-order scheme.

<sup>&</sup>lt;sup>1</sup> Department of Mechanical and Aerospace Engineering, Hong Kong University of Science and Technology, Hong Kong SAR.

<sup>&</sup>lt;sup>2</sup> State Key Laboratory for Strength and Vibration of Mechanical Structures, Shaanxi Key Laboratory of Environment and Control for Flight Vehicle, School of Aerospace Engineering, Xi'an Jiaotong University, China.

<sup>&</sup>lt;sup>3</sup> Department of Mathematics, Hong Kong University of Science and Technology, Hong Kong SAR.

<sup>&</sup>lt;sup>4</sup> Shenzhen Research Institute, Hong Kong University of Science and Technology, Shenzhen, China.

<sup>&</sup>lt;sup>5</sup> Department of Mechanical and Aerospace Engineering, Southern University of Science and Technology, Shenzhen 518055, China.

<sup>\*</sup>Corresponding author. *Email addresses:* clicz@connect.ust.hk (C. Li), jixing@xjtu.edu.cn (X. Ji), makxu@ust.hk (K. Xu), wanglp@sustech.edu.cn (L. P. Wang)

## 1 Introduction

The development of high-order schemes for compressible flows has achieved great success in resolving complex vortex structures and capturing flow discontinuities. Compared with the finite difference method, the high-order finite-volume method has greatly improved. The finite volume method comprises the three main substeps, namely, the spatial reconstruction, flux evaluation, and temporal discretization. Most of the efforts were focused on building a novel high-order reconstruction method, which indeed achieved great success. The successful high-order reconstruction methods include the essentially non-oscillatory (ENO) and weighted essentially non-oscillatory (WENO) scheme [11, 16, 21]. There exist many modified versions of WENO, such as WENO-JS [16], WENO-Z [3], WENO with adaptive order WENO-AO [1], multi-resolution WENO [38], and target ENO(TENO) [8], etc.

In addition to the reconstruction, the flux evaluation and temporal discretization method also play dominant roles in the overall performance of the scheme. Generally, in terms of the flux solver, the approximate Riemann solvers are commonly used, such as Roe [25], Advection Upstream Splitting Method (AUSM) [20], and Harten-Lax-van Leer contact (HLLC) [30]. Since the Riemann solvers with a forward-Euler step has only a first-order temporal accuracy, the Runge-Kutta (RK) method [12] is usually adopted to advance the solution in time, making the high-order schemes stable and accurate in time.

Different from the Riemann solvers, there are other flux solvers to treat the timedependent interface fluxes, such as generalized Riemann problem (GRP) [19], Arbitrary accuracy DERivative (ADER) [26], the gas-kinetic scheme (GKS), etc. In this paper, we mainly focus on the GKS solver. During the past two decades, GKS has shown its ability to accurately recover the Euler and Navier-Stokes solutions [34, 36]. GKS is mainly based on the Bhatnagar-Gross-Krook (BGK) collision model [2] and by directly integrating the BGK Boltzmann equation along the trajectory line, a time-dependent gas distribution function can be obtained, which has the advantage of high order in time and space. By using the time-dependent gas distribution function at the cell interface, the cell interface flux can be updated. In the previous study, it was found that the advantages of high-order GKS (HGKS) are as follows: (1) GKS presents a gas flow evolution from the kinetic scale to hydrodynamic scale, which not only provides accurate solutions for the smooth regions of the flow field but also effectively captures shockwaves in the discontinuous regions; (2) the inviscous and viscous terms are obtained simultaneously from the gas distribution function containing both equilibrium and non-equilibrium flow properties; (3) the flux in GKS has multi-dimensional properties [36], with contributions from both normal and tangential derivatives of flow variables around a cell interface; (4) compared with the traditional time-space independent Riemann Solver, the multistage multi-derivative (MSMD) [15] methods such as the two-stage fourth-order scheme (S2O4) [24] can provide the same order time integration accuracy with fewer middle stages due to the considerations of the time-derivative of the interface flux in GKS.

In the previous work, Yang compared the performance of GKS and HLLC flux us-

ing the same high-order reconstruction and found that with the same mesh and CFL number, WENO5-AO-GKS shows better performance in shock and contact wave capturing than WENO5-AO-HLLC. [37]. To find out whether the spatial reconstruction or flux solver contributes more to the overall accuracy of the simulated complex flows containing shock-vortex interactions, this paper will compare the performance of different flux solvers under the same reconstruction or different reconstructions under the same flux solver.

Since the fifth-order reconstruction methods are widely used in various studies [14, 23], the finite volume schemes of fifth-order space accuracy are selected for comparison. Specifically, we shall select two traditional Riemann fluxes (Lax-Friderich (L-F) and HLLC) and GKS flux, along with two reconstruction methods: WENO5-Z and TENO5. The specific combination of L-F and WENO5-Z will be viewed as the baseline for comparisons. Besides, S2O4 temporal discretization is used for GKS, and fourth-order Runge-Kutta (RK4) is adopted for L-F and HLLC solver, while both time marching schemes achieve the same temporal accuracy. L-F is widely used in high-order schemes due to its simplicity and robustness, WENO5-Z balances accuracy and robustness better than traditional WENO methods like WENO-JS [4]. GKS and TENO5 are more recent developments in high-order flux and reconstruction: GKS can balance accuracy and robustness through its multi-scale gas distribution function and TENO with its novel cut-off weighting strategy can greatly reduce the numerical dissipation while preserving the sharp shock-capturing property. TENO has been applied to multi-phase flows [10] and turbulence flows [9] in recent years.

In the one-dimensional and two-dimensional flows to be simulated in this paper, the low-dissipation TENO reconstruction has shown its ability to better capture high wave number flow structures than WENO-Z. However, TENO has less effects on improving the performance of the GKS. The possible reason is that spatial derivatives participate in the local gas evolution in GKS and are not very sensitive to the interface pointwise values. The numerical flux formulation plays an important role in a high-order scheme when dealing with physical processes with strong nonlinearity. Choosing a better flux formulation (such as GKS) might be more important than choosing a better spatial reconstruction method when balancing the accuracy in resolving small-scale waves and the robustness in treating strong discontinuities.

This paper is organized as follows. In Section 2, the classic finite volume method is introduced. Section 3 presents the traditional Riemann solvers, including Lax-Friedrichs and HLLC Riemann solver, spatial reconstruction including WENO5-Z and TENO5, and the Runge-Kutta method for time integration. Section 4 presents the high-order GKS method, including the gas-kinetic scheme, spatial reconstruction, and two-stage fourth-order temporal discretization. Section 5 provides the simulation results for WENO-GKS, TENO-GKS, WENO-HLLC, and TENO-HLLC schemes. Section 6 contains a discussion and the last section summarizes the conclusions.

## 2 Standard finite volume method

In this section, the formulation of the classical finite-volume method is presented.

To facilitate presentation, we consider the one-dimensional scalar hyperbolic conservation equation

$$\frac{\partial u}{\partial t} + \frac{\partial}{\partial x} F(u) = 0, \tag{2.1}$$

where u(x,t) denotes the conservative variable and F(u) denotes the flux function. After discretising Eq. (2.1) on uniform cell elements, e.g.,  $I_i = [x_{i-1/2}, x_{i+1/2}]$  and  $\Delta x = x_{i+1/2} - x_{i-1/2}, i = 0, \dots, N$ , a system of ordinary differential equations

$$\frac{\partial \bar{u}_i}{\partial t} = -\frac{1}{\Delta x} \int_{x_i - \Delta x/2}^{x_i + \Delta x/2} \frac{\partial F}{\partial x} dx, \quad i = 0, \dots, N,$$
(2.2)

where  $\bar{u}_i$  denotes the volume-averaged conservative variable in cell element  $I_i$ ,

$$\bar{u}_i = \frac{1}{\Delta x} \int_{x_i - \Delta x/2}^{x_i + \Delta x/2} u(x) dx.$$
 (2.3)

Eq. (2.2) can be further approximated by a conservative finite-volume method as

$$\frac{\mathrm{d}\bar{u}_i}{\mathrm{d}t} \approx -\frac{1}{\Delta x} (\hat{F}_{i+1/2} - \hat{F}_{i-1/2}),\tag{2.4}$$

where the numerical flux  $\hat{F}_{i+1/2}$  at the cell interface is computed by a Riemann solver

$$\hat{F}_{i+1/2} = F_{i+\frac{1}{2}}^{\text{Riemann}}(u_{i+1/2}^L, u_{i+1/2}^R), \tag{2.5}$$

and the left-side data  $u_{i+1/2}^L$  and the right-side data  $u_{i+1/2}^R$  are computed by the left-biased and right-biased reconstruction, respectively. Based on this framework, Godunov presented a first-order time-integration scheme for Euler equations

$$\bar{u}_i^{n+1} = \bar{u}_i^n + \frac{\Delta t}{\Delta x} (\hat{F}_{i-1/2} - \hat{F}_{i+1/2}). \tag{2.6}$$

For different types of high-order finite volume methods, the accuracy of the updated solution depends critically on the interface flux function  $\hat{F}_{i+1/2}$ , which depends on the interface reconstruction data,  $u_{i+1/2}^L$ ,  $u_{i+1/2}^R$ , and the functional form for the flux at the cell interface,  $F_{i+1/2}^{\rm Riemann}$ .

# 3 Riemann-solver-based high-order finite volume scheme

Although we can solve the exact solution of a Riemann problem at the cell interface, approximate Riemann solvers are still widely used because of its high efficiency. [29] For

different approximate Riemann solvers, e.g., the LF flux, the Roe flux and the HLLC flux, they can all be formulated in a general form as [7]

$$F_{i+\frac{1}{2}}^{\text{Riemann}}(u_{i+1/2}^{L}, u_{i+1/2}^{R}) = \frac{1}{2}(F(u_{i+1/2}^{L}) + F(u_{i+1/2}^{R})) - |\tilde{\delta}_{i+1/2}|(u_{i+1/2}^{R} - u_{i+1/2}^{L}), \quad (3.1)$$

where  $\tilde{\partial}_{i+1/2}$  means the characteristic signal velocity evaluated at the cell interface. The first term in Eq. (3.1) is a central scheme,

$$\frac{1}{2}(F(u_{i+1/2}^L)+F(u_{i+1/2}^R)),$$

which is a non-dissipative term. The second term in Eq. (3.1),

$$|\tilde{\partial}_{i+1/2}|(u_{i+1/2}^R-u_{i+1/2}^L),$$

which denotes the numerical dissipation. The numerical dissipation is derived from two sources, i.e., the difference between  $u_{i+1/2}^R$  and  $u_{i+1/2}^L$  which is computed by the high-order reconstruction and the scaling coefficient  $|\tilde{\delta}_{i+1/2}|$  which is determined differently for different Riemann solvers.

In smooth regions, the higher-order reconstruction should show no data jump between  $u_{i+1/2}^R$  and  $u_{i+1/2}^L$  and as such a minimal numerical dissipation. In the meantime, for distinct Riemann solvers, the scaling coefficients  $|\tilde{\delta}_{i+1/2}|$  are different generating different levels of nonlinear dissipation.

In the following section, the Riemann-solver-based high-order finite volume schemes, which involve the Lax-Friedrichs, HLLC Riemann solver, and high-order TENO, WENO reconstruction method, are introduced in detail.

#### 3.1 Traditional Riemann solvers

#### 3.1.1 The Lax-Friedrichs solver

The Lax-Friedrichs method is used to obtain the flux term in WENO5-LF and TENO5-LF schemes. A nonlinear hyperbolic conservation law is defined through a flux function **F**:

$$\mathbf{W}_t + \mathbf{F}_x(\mathbf{W}) = 0. \tag{3.2}$$

For the two-dimensional Euler equations, the conservative variables **W** and the corresponding fluxes **F** are,

$$\mathbf{W} = [\rho, \rho u, \rho v, \rho E]^T, \quad \mathbf{F} = [\rho u, \rho u^2 + p, \rho u v, u(\rho E + p)]^T. \tag{3.3}$$

The generalization of the Lax-Friedrichs method to nonlinear systems takes the form [18]

$$\mathbf{W}_{i}^{n+1} = \mathbf{W}_{i}^{n} - \frac{\Delta t}{\Delta x} (\mathbf{F}(\mathbf{W}_{i+1/2}^{n}) - \mathbf{F}(\mathbf{W}_{i-1/2}^{n})), \tag{3.4}$$

with the Lax-Friedrichs interface flux given by

$$\mathbf{F}(W_{i+1/2}) = \frac{1}{2} (\mathbf{F}_i^n + \mathbf{F}_{i+1}^n) + \frac{\Delta x}{2\Delta t} (\mathbf{W}_i^n - \mathbf{W}_{i+1}^n), \tag{3.5}$$

where  $\mathbf{F}_{i}^{n}$  is the corresponding flux in Eq. (3.3).

#### 3.1.2 HLLC Riemann solver

The HLLC Riemann solver [30] is used to obtain the flux term in the current WENO5-HLLC and TENO5-HLLC scheme. HLLC solver is an approximate Riemann solver, which consists of four constant states. Assume that the speeds of the slowest and fastest waves are  $S_L$  and  $S_R$ , and the speed of the middle shear wave is  $S_*$ . Then, the HLLC solver can be written as follows,

$$\mathbf{W}(x,t) = \begin{cases} \mathbf{W}_{L}, & S_{L} \ge 0, \\ \mathbf{W}_{*L}, & S_{L} \le 0 \le S_{*}, \\ \mathbf{W}_{*R}, & S_{*} \le 0 \le S_{R}, \\ \mathbf{W}_{R}, & S_{R} \le 0, \end{cases}$$
(3.6)

and the corresponding numerical flux can be defined as,

$$\mathbf{F}_{i+1/2} = \begin{cases} \mathbf{F}_{L}, & 0 \le S_{L}, \\ \mathbf{F}_{*L}, & S_{L} \le 0 \le S_{*}, \\ \mathbf{F}_{*R}, & S_{*} \le 0 \le S_{R}, \\ \mathbf{F}_{R}, & 0 \ge S_{R}, \end{cases}$$
(3.7)

where  $F_L = F(W_L)$ ,  $F_R = F(W_R)$  by Eq. (3.3) and  $\mathbf{F}_{*K} = \mathbf{F}_K + S_L(\mathbf{W}_{*K} - \mathbf{W}_K)$ , K = L, R. The  $\mathbf{W}_{*K}$ , K = L, R, is given by,

$$\mathbf{W}_{*K} = \rho_K \left( \frac{S_K - U_K}{S_K - S_*} \right) \begin{bmatrix} 1 \\ S_* \\ V_K \\ \frac{E_K}{\rho_K} + (S_* - U_K) \left[ S_* + \frac{p_K}{\rho_K (S_K - U_K)} \right] \end{bmatrix},$$
(3.8)

where  $S_*$  is related to the speeds  $S_L$  and  $S_R$ , namely

$$S_* = \frac{p_R - p_L + \rho_L U_L (S_L - U_L) - \rho_R U_R (S_R - U_R)}{\rho_L (S_L - U_L) - \rho_R (S_R - U_R)}.$$
(3.9)

There are many methods to estimate wave speeds  $S_L$  and  $S_R$ , and a pressure-based wave speed estimate method proposed by Toro is adopted in the current work [29]. Firstly, we need to estimate  $p_*$ , the pressure of the region  $x/t \in [S_L, S_R]$ . Based on the Two-Rarefaction Riemann solver (TRRS), the estimated  $p_*$  is

$$p_* = \left[ \frac{a_L + a_R - \frac{\gamma - 1}{2} (U_R - U_L)}{a_L / p_L^z + a_R / p_R^z} \right]^{1/z}, \tag{3.10}$$

where  $z = (\gamma - 1)/(2\gamma)$ , and  $\gamma$  is the specific heat ratio. Then, the speeds  $S_L$  and  $S_R$  are coming from the exact wave-speed relations in the exact Riemann solver,

$$S_L = U_L - a_L q_L, \quad S_R = U_R + a_R q_R,$$
 (3.11)

where  $a_L$ ,  $a_R$  are the sound speeds of the initial left and right state, and  $q_K$ , K = L, R, are

$$q_{K} = \begin{cases} 1, & p_{*} \leq p_{K}, \\ \left[1 + \frac{\gamma + 1}{2\gamma} (p_{*}/p_{K} - 1)\right]^{1/2}, & p_{*} > p_{K}. \end{cases}$$
(3.12)

#### 3.2 WENO5-Z reconstruction for traditional Riemann solver

The above time evolution solution is based on the high-order initial reconstruction for macroscopic flow variables. The fifth-order WENO reconstruction is adopted in this study.

The key idea of WENO is to construct the desired values Q on targeted locations by the linear combination of the sub-stencil values through the optimal weights. To reconstruct the left interface value  $Q_{i+1/2}^l$  at the cell interface  $x_{i+1/2}$ , three sub-stencils are selected

$$S_0 = [I_{i-2}, I_{i-1}, I_i], \quad S_1 = [I_{i-1}, I_i, I_{i+1}], \quad S_2 = [I_i, I_{i+1}, I_{i+2}].$$

The quadratic polynomials  $p_k^{r3}(x)$  corresponding to the sub-stencils  $S_k$ , k = 0,1,2 are constructed by requiring

$$\frac{1}{\Delta x} \int_{I_{i-j-k-1}} p_k^{r3}(x) dx = \overline{Q}_{i-j-k-1}, \quad j = -1, 0, 1,$$
(3.13)

where  $\overline{Q}$  is the cell-averaged value. Each of them can achieve a third-order (r=3) spatial accuracy in the smooth case in their sub-stencil. For the reconstructed polynomials, the point value at the cell interface  $x_{i+1/2}$  is given in terms of the cell averages as follows

$$p_0^{r3}(x_{i+1/2}) = \frac{1}{3}\overline{Q}_{i-2} - \frac{7}{6}\overline{Q}_{i-1} + \frac{11}{6}\overline{Q}_i, \tag{3.14}$$

$$p_1^{r3}(x_{i+1/2}) = -\frac{1}{6}\overline{Q}_{i-1} + \frac{5}{6}\overline{Q}_i + \frac{1}{3}\overline{Q}_{i+1}, \tag{3.15}$$

$$p_2^{r3}(x_{i+1/2}) = \frac{1}{3}\overline{Q}_i + \frac{5}{6}\overline{Q}_{i+1} - \frac{1}{6}\overline{Q}_{i+2}.$$
 (3.16)

The smooth indicators for  $p^{r3}$  are given as:

$$\beta_0 = \frac{13}{12} (\overline{Q}_{i-2} - 2\overline{Q}_{i-1} + \overline{Q}_i)^2 + \frac{1}{4} (\overline{Q}_{i-2} - 4\overline{Q}_{i-1} + 3\overline{Q}_i)^2, \tag{3.17}$$

$$\beta_1 = \frac{13}{12} (\overline{Q}_{i-1} - 2\overline{Q}_i + \overline{Q}_{i+1})^2 + \frac{1}{4} (\overline{Q}_{i-1} - \overline{Q}_{i+1})^2, \tag{3.18}$$

$$\beta_2 = \frac{13}{12} (\overline{Q}_i - 2\overline{Q}_{i+1} + \overline{Q}_{i+2})^2 + \frac{1}{4} (3\overline{Q}_i - 4\overline{Q}_{i+1} + \overline{Q}_{i+2})^2.$$
 (3.19)

To avoid the loss of the order of accuracy at inflection points, in this paper, we use the nonlinear weights in WENO-Z [3], which are

$$\omega_k = \gamma_k \left( 1 + \frac{\tau}{\beta_k + \epsilon} \right), \tag{3.20}$$

where the global smooth indicator  $\tau$  is defined as

$$\tau = |\beta_2 - \beta_0|$$

and  $\gamma_0 = \frac{1}{10}$ ,  $\gamma_1 = \frac{6}{10}$ ,  $\gamma_3 = \frac{3}{10}$  are defined as optimal weights. The normalized weights are given by

$$\overline{\omega_k} = \frac{\omega_k}{\sum_{q=0}^2 \omega_q}.$$
(3.21)

Then all the desired quantities at cell left interfaces can be fully determined as follows,

$$Q_{i+1/2}^{l} = \sum_{k=0}^{2} \overline{\omega_k} p_k^{r3}(x_{i+1/2}). \tag{3.22}$$

The same strategy is applied to the right side of the interface.

#### 3.3 TENO5 reconstruction

For a five-point TENO scheme, the involved candidate stencils  $[p_0, p_1, p_2]$  are the same as for the WENO5. The smooth indicators  $[\beta_0, \beta_1, \beta_2]$  are also the same as WENO5.

## 3.3.1 Scale separation

The smoothness measure which is used for scale separation of discontinuities from smooth waves is defined as

$$\gamma_k = \left(C + \frac{\tau_K}{\beta_k + \epsilon}\right)^q, \quad k = 0, 1, 2,$$

where  $\epsilon = 10^{-40}$  to avoid a zero denominator. The parameters q = 6 and C = 1 are used for strong scale separation.  $\tau_K$  measures the smoothness of the full-size stencil.

## 3.3.2 ENO-like stencil selection strategy

The smoothness measure is normalized first as

$$\chi_k = \frac{\gamma_k}{\sum_{k=0}^2 \gamma_k},\tag{3.23}$$

and then subjected to a sharp cutoff function

$$\delta_k = \begin{cases} 0, & \text{if } \chi_k < C_T, \\ 1, & \text{otherwise.} \end{cases}$$
 (3.24)

The non-dimensional parameter  $C_T$  determines whether or not a stencil is recognized as "smooth". The cutoff function ensures that a candidate stencil is fully suppressed for the final reconstruction if the measured smoothness is below a certain threshold, otherwise, it is adopted with its original weight. The choice of the threshold  $C_T$  can be determined from a compromise between good spectral properties and numerical robustness for discontinuity detection through numerical experiments.

To remove contributions from candidate stencils containing discontinuities, the optimal weight  $d_k$  subjected to the cut-off  $\delta_k$  is re-normalized as

$$w_k = \frac{d_k \delta_k}{\sum_{k=0}^2 d_k \delta_k},\tag{3.25}$$

so that the contributions from stencils containing discontinuities vanish. The final k-th order reconstructed numerical flux evaluated at cell faces  $i+\frac{1}{2}$  is assembled as

$$Q_{i+1/2}^{l} = \sum_{k=0}^{2} \omega_k p_k^{r3}(x). \tag{3.26}$$

Since the  $\delta_k$  function switches between 0 and 1, a smooth transition from high-order to low-order through the weighting strategy is prevented. Nevertheless, the result can achieve arbitrarily high-order accuracy while satisfying the ENO property.

#### 3.4 Viscous flux term

For viscous flow problems, the computation of viscous fluxes in the Navier-Stokes equations is essential. In the current HLLC and LF scheme, both the conservative variables  $Q_{i+1/2}$  and the corresponding derivatives  $(Q_x)_{i+1/2}$  at the cell interface need to be constructed by the cell averaged conservative variables  $\overline{Q}$ . In this paper, a sixth-order central difference method is applied for the calculation of viscous fluxes. The conservative variables can be written as follows

$$Q_{i+1/2} = \frac{1}{60} (\overline{Q}_{i-2} - 8\overline{Q}_{i-1} + 37\overline{Q}_i + 37\overline{Q}_{i+1} - 8\overline{Q}_{i+2} + \overline{Q}_{i+3}),$$

and the corresponding derivatives are,

$$(Q_x)_{i+1/2} = \frac{1}{180\Delta x} (-2\overline{Q}_{i-2} + 25\overline{Q}_{i-1} - 245\overline{Q}_i + 245\overline{Q}_{i+1} - 25\overline{Q}_{i+2} + 2\overline{Q}_{i+3}).$$

For two-dimensional problems, the dimension-by-dimension strategy is adopted [1,2]. The reconstructed value  $Q_{i+1/2,j_l}$  at the Gaussian quadrature point  $j_l$ , the corresponding normal derivative  $(Q_x)_{i+1/2,j_l}$ , and tangential derivative  $(Q_y)_{i+1/2,j_l}$  can be obtained by the fourth-order polynomial  $p^{r5}(y)$  based on the above  $Q_{i+1/2}$  and  $(Q_x)_{i+1/2}$ . Then, all terms in the viscous fluxes can be fully determined. A similar procedure can be easily extended to three-dimensional problems."

## 3.5 Time marching method

The classical fourth-order Runge-Kutta method (RK4) is applied for time integration in a traditional Riemann solver scheme for achieving the 4th-order temporal accuracy. The RK4 time marching method is adopted as follows,

$$w^1 = w^n + \frac{1}{2}\Delta t \mathbf{L}(w^n), \tag{3.27}$$

$$w^2 = w^n + \frac{1}{2}\Delta t \mathbf{L}(w^1),$$
 (3.28)

$$w^3 = w^n + \Delta t \mathbf{L}(w^2), \tag{3.29}$$

$$w^{n+1} = w^n + \frac{1}{6} (\Delta t \mathbf{L}(w^n) + 2\Delta t \mathbf{L}(w^1) + \Delta t \mathbf{L}(w^2) + \Delta t \mathbf{L}(w^3)). \tag{3.30}$$

Finally, a block diagram of the solution procedure for a traditional Riemann-solver-based high-order finite volume scheme is given in Fig. 1.

# 4 Gas-kinetic-solver-based high-order finite volume scheme

In this section, the formulation of GKS is introduced. To show its ability to handle mutidimensionality, the 2-D case is presented in detail.

#### 4.1 Gas-Kinetic Scheme

The two-dimensional gas-kinetic BGK equation can be written as [2]

$$f_t + \mathbf{u} \cdot \nabla f = \frac{g - f}{\tau},\tag{4.1}$$

where  ${\bf u}$  is the particle velocity, f is the gas distribution function, g is the corresponding equilibrium state, and  $\tau$  is the collision time. The equilibrium state is a Maxwellian distribution

$$g = \rho \left(\frac{\lambda}{\pi}\right)^{\frac{K+2}{2}} e^{\lambda((u-U)^2)+(v-V)^2+\xi^2)},$$

where  $\lambda=m/2kT$ , and m,k,T represents the molecular mass, the Boltzmann constant, and temperature, K is the number of internal degrees of freedom, i.e.,  $K=(4-2\gamma)/(\gamma-1)$  for two-dimensional flows, and the  $\gamma$  is the specific heat ratio,  $\xi$  is the internal variables with  $\xi^2=\xi_1^2+\cdots+\xi_K^2$ ,  $d\Xi=dudvd\xi_1\cdots d\xi_K$ . Due to the conservation of mass, momentum, and energy during particle collisions, The collision term satisfies the following compatibility condition

$$\int \frac{g - f}{\tau} \psi d\Xi = 0, \tag{4.2}$$

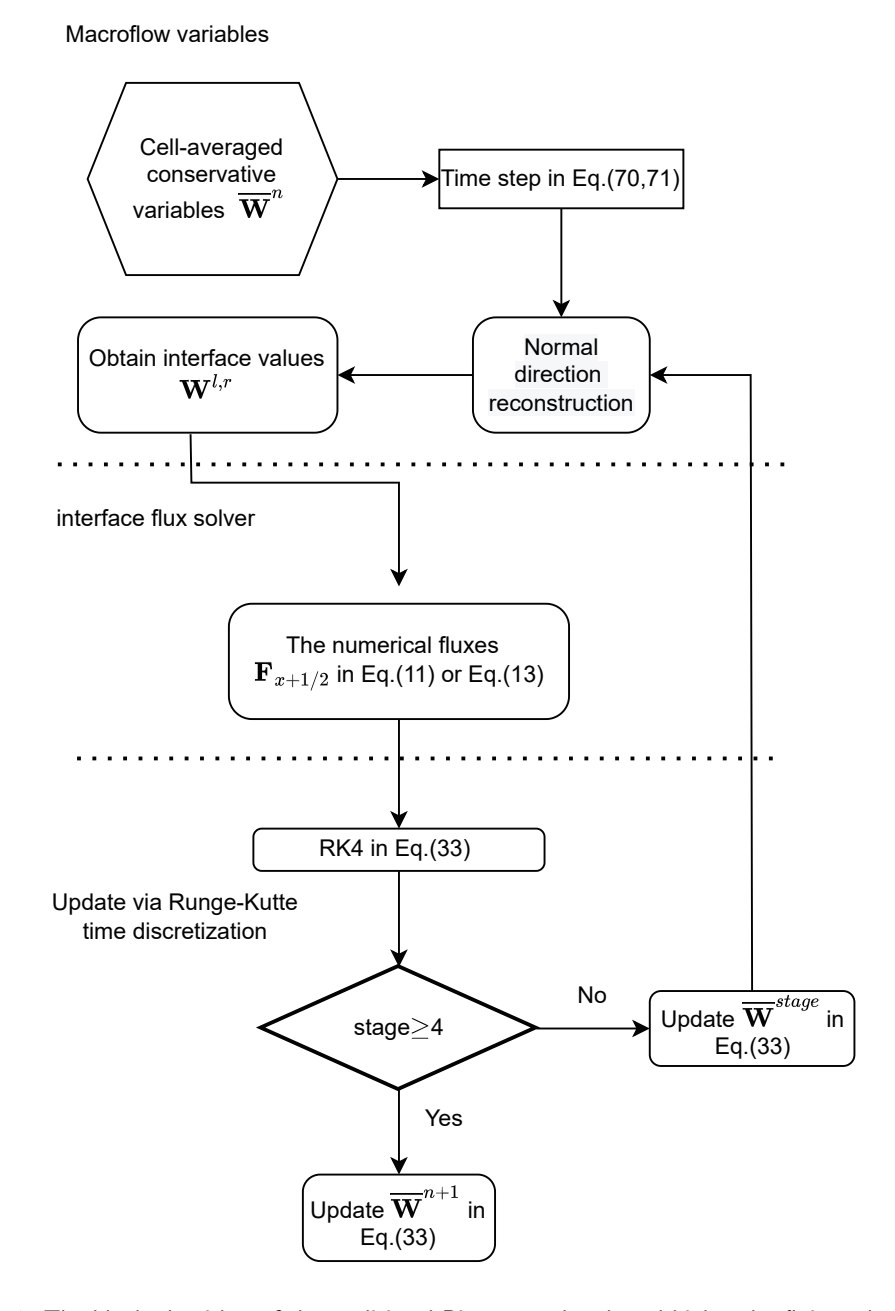


Figure 1: The block algorithm of the traditional Riemann-solver-based high-order finite volume scheme.

where  $\psi = (1, u, v, \frac{1}{2}(u^2 + v^2 + \xi^2))^T$ , The connections between macroscopic conservative flow variables  $W = (\rho, \rho U, \rho V, \rho E)^T$  with the distribution function f are

$$W = \int f \boldsymbol{\psi} d\Xi. \tag{4.3}$$

Taking moments of the BGK equation (4.1) and integrating with respect to a discrete space volume  $S_{ij} = [x_i - \Delta x/2, x_i + \Delta x/2] \times [y_j - \Delta y/2, y_j + \Delta y/2]$ , the semi-discrete finite volume scheme can be written as

$$\frac{dW_{ij}}{dt} = -\frac{1}{\Delta x} (\mathbf{F}_{i+1/2,j}(t) - \mathbf{F}_{i-1/2,j}(t)) - \frac{1}{\Delta y} (\mathbf{G}_{i,j+1/2}(t) - \mathbf{G}_{i,j-1/2}(t)), \tag{4.4}$$

where  $\mathbf{F}_{i\pm 1/2,j}(t)$  and  $\mathbf{G}_{i,j\pm 1/2}(t)$  are the time dependent numerical fluxes at cell interface in x and y direction. To achieve accuracy in space, the Gaussian quadrature is used, such that

$$\mathbf{F}_{i+1/2,j}(t) = \frac{1}{\Delta y} \int_{y_{i-1/2}}^{y_{j+1/2}} \mathbf{F}_{i+1/2}(y,t) dy = \sum_{\ell=1}^{2} \omega_{\ell} \mathbf{F}_{i+1/2,j_{\ell}}(t), \tag{4.5}$$

where  $\omega_1 = \omega_2 = 1/2$  are weights for the Gaussian quadrature points  $y_{j_\ell} = y_j + \frac{(-1)^\ell}{2\sqrt{3}} \Delta y$ ,  $\ell = 1, 2$ , to achieve fourth-order accuracy.  $\mathbf{F}_{i+1/2, j_\ell}$  are the numerical fluxes in the Gaussian quadrature point.

$$\mathbf{F}_{i+1/2,j_{\ell}}(t) = \int \psi u f(x_{i+1/2}, y_{j_{\ell}}, t, u, v, \xi) d\Xi, \tag{4.6}$$

where  $f(x_{i+1/2}, y_{j_\ell}, t, u, v, \xi)$  is the gas distribution function at the cell interface. By integrating the BGK equation Eq. (4.1), the general solution f can be obtained.

$$f(x_{i+1/2}, y_{\ell}, t, u, v, \xi) = \frac{1}{\tau} \int_0^t g(x', y', t', u, v, \xi) e^{-(t-t')/\tau} dt' + e^{-t/\tau} f_0(-ut, -vt, u, v, \xi), \quad (4.7)$$

for simplification of notation,  $(x_{j+1/2}, y_\ell) = (0,0)$ ,  $x_{i+1/2} = x' + u(t-t')$ ,  $y_{j_\ell} = y' + v(t-t')$  are the trajectory of particles.  $f_0$  is the initial gas distribution function, and g is the corresponding equilibrium state.

In the integral solution Eq. (4.7), the initial gas distribution function can be constructed as

$$f_0 = f_0^l(x, y, u, v)H(x) + f_0^r(x, y, u, v)(1 - H(x)),$$
(4.8)

where H(x) is the Heaviside function,  $f_0^l$  and  $f_0^r$  are the initial gas distribution function on the left and right side of the interface at t=0, which can be determined by the initial macroscopic variables. The initial distribution function  $f_0^k$ , k=l,r in the space around (x,y)=(0,0), can be expressed as

$$f_0^k = g^k (1 + a^k x + b^k y - \tau (a^k u + b^k v + A^k)), \quad k = l, r,$$
(4.9)

where  $g^k$ , k=l,r are the Maxwellian distribution functions on the left and right-hand sides of the cell interface, which correspond to the macroscopic flow variables  $W^k$ , k=l,r. The coefficients  $a^k$ ,  $b^k$ , k=l,r are related to the slopes in space in the expansion of a Maxwellian

in the normal and tangential direction, which can be obtained from the derivatives of the macroscopic variables,

$$\langle a^k \rangle = \partial W^k / \partial x, \quad \langle b^k \rangle = \partial W^k / \partial y, \quad k = l, r,$$
 (4.10)

where  $\langle \cdots \rangle$  means taking the moments of the Maxwellian distribution function,

$$\langle \cdots \rangle = \int \psi(\cdots) g d\Xi.$$

The time evolution coefficient  $A^k$ , k=l,r, related to non-equilibrium parts in Eq. (4.9), can be determined by compatibility condition.

$$\langle a^k u + b^k v + A^k \rangle = 0, \quad k = l, r. \tag{4.11}$$

After the determination of  $f_0$ , the equilibrium state g at the interface can be constructed with spatial and temporal coefficients as

$$g = g^{c} (1 + \overline{a}x + \overline{b}y + \overline{A}t), \tag{4.12}$$

where  $g^c$  is the local equilibrium at  $(x = x_{j+1/2}, t = 0)$ .  $g^c$  and corresponding coefficients  $\overline{a}, \overline{b}, \overline{A}$  can be given by the compatibility condition,

$$\int \psi g^c d\Xi = \mathbf{W}^{\mathbf{e}} = \int_{u>0} \psi g^l d\Xi + \int_{u<0} \psi g^r d\Xi, \tag{4.13a}$$

$$\int \psi \overline{a} g^c d\Xi = \partial \mathbf{W}^{\mathbf{e}} / \partial x = \int_{u > 0} \psi a^l g^l d\Xi + \int_{u < 0} \psi a^r g^r d\Xi, \tag{4.13b}$$

$$\int \psi \overline{b} g^c d\Xi = \partial \mathbf{W}^{\mathbf{e}} / \partial y = \int_{\mathbb{R}^3} \psi b^l g^l d\Xi + \int_{\mathbb{R}^3} \psi b^r g^r d\Xi, \tag{4.13c}$$

$$\langle \overline{a}u + \overline{b}v + \overline{A} \rangle = 0,$$
 (4.13d)

where  $W^e$  are the macroscopic variables corresponding to the equilibrium state  $g^c$ .

After constructing the initial gas distribution  $f_0$  and equilibrium state g at the interface, time-dependent distribution function  $f(0,y,t,u,\psi)$  at a cell interface can be obtained by substituting (4.12) and (4.9) into (4.7),

$$f(0,y,t,u,v,\psi) = (1 - e^{-t/\tau_n})g^c + (t+\tau)e^{-t/\tau_n} - \tau)(ug_x^c + vg_x^c) + (t-\tau+\tau e^{-t/\tau_n})\bar{A}g^c + e^{-t/\tau_n}[g^l - (ug_x^l + vg_y^l)(\tau+t) - \tau A_l]H(u) + e^{-t/\tau_n}[g^r - (ug_x^r + vg_y^r)(\tau+t) - \tau A_r](1 - H(u)).$$

$$(4.14)$$

For smooth flow, the time-dependent solution in Eq. (4.14) can be simplified as

$$f(0,y,t,u,v,\psi) = g^{c} - \tau(g_{x}^{c}u + g_{t}^{c}) + tg_{t}^{c}. \tag{4.15}$$

For the inviscid flow, the collision time  $\tau$  is

$$\tau = c_1 \Delta t + c_2 \left| \frac{p_l - p_r}{p_l + p_r} \right| \Delta t, \tag{4.16}$$

where  $c_1 = 0.01$  and  $c_2 = 1 \sim 5$ . For the viscous flow, the collision time is related to the viscosity coefficient,

$$\tau = \frac{\mu}{p} + c_2 \left| \frac{p_l - p_r}{p_l + p_r} \right| \Delta t, \tag{4.17}$$

where  $p_l$  and  $p_r$  denote the pressure on the left and right sides of the cell interface,  $\mu$  is the dynamic viscous coefficient, and p is the pressure at the interface. In the smooth flow regions, it reduces to  $\tau = \mu/p$ .

## 4.2 Spatial reconstruction for gas-kinetic scheme

#### 4.2.1 1-Dimensional reconstruction

In 1-D case, the standard WENO5-Z reconstruction and TENO5 reconstruction applied to the cell interface value  $w^l$ ,  $w^r$  for GKS is the same as what is described in Section 3.2.

#### 4.2.2 2-Dimensional reconstruction

In 2-D case, the reconstruction is conducted direction by direction. In this part, we denote  $\bar{w}$  as cell average value,  $\cap w$  as line average value, and w as pointwise values. For the superscript,  $w^l$ ,  $w^r$  represent the reconstructed value on the left or right sides of a cell interface, which is related to the non-equilibrium part  $g^l$  and  $g^r$  in GKS in Eq. (4.14). Then  $w^e$  is the reconstructed equilibrium state. Before the reconstruction, for cell (i,j), the cell average value  $\bar{w}$  is stored. And after the reconstruction, the output we need is

$$w^{l}, w^{r}, w^{e}, \quad w^{l}_{x}, w^{r}_{x}, w^{e}_{x}, \quad w^{l}_{xx}, w^{r}_{xx}, w^{e}_{xx}, \quad w^{l}_{y}, w^{r}_{y}, w^{e}_{y}, \quad w^{l}_{yy}, w^{r}_{yy}, w^{e}_{yy}, \quad w^{r}_{yy}, w^{$$

at each Gaussian point.

 $w_x^{l,r}$  are obtained by constructing a second order polynomial by requiring

$$\frac{1}{\Delta x} \int_{I_i} p(x) dx = \overline{w}_i, \quad p(x_{i-1/2}) = w_{i-1/2}^r, \quad p(x_{i+1}) = w_{i+1/2}^l.$$

And we finally get

$$p(x) = a_0 + a_1(x - x_i) + a_2(x - x_i)^2,$$
  $a_0 = \frac{1}{4}(-w_{i-1/2}^r - w_{i+1/2}^l + 6w_i),$  (4.18)

$$a_1 = \frac{w_{i+1/2}^l - w_{i-1/2}^r}{\Lambda h}, \qquad a_2 = \frac{3(w_{i+1/2}^l + w_{i-1/2}^r - 2w_i)}{\Lambda h^2}. \tag{4.19}$$

Thus,

$$(w_x^r)_{i-1/2} = -\frac{2(2w_{i-1/2}^r + w_{i+1/2}^l - 3w_i)}{\Delta h}, \quad (w_x^l)_{i+1/2} = -\frac{2(w_{i-1/2}^r + 2w_{i+1/2}^l - 3w_i)}{\Delta h}.$$

The procedure of the two-dimensional reconstruction is shown in Algorithm 1.

## Algorithm 1: Two-dimensional reconstruction algorithm.

```
Input: Cell average values \bar{w^n}
          Output: interface gaussian points values and slopes
                                       \bar{w}_{i+1/2,i+2}^l, \partial_x w_{i+1/2,i_l}^l, \partial_{xx} w_{i+1/2,i_l}^l, \partial_y w_{i+1/2,i_l}^l, \partial_{yy} w_{i+1/2,i_l}^l,
                                       \overline{w}_{i+1/2,j+2}^{r}, \partial_{x} w_{i+1/2,j_{l}}^{r}, \partial_{xx} w_{i+1/2,j_{l}}^{r}, \partial_{y} w_{i+1/2,j_{l}}^{r}, \partial_{yy} w_{i+1/2,j_{l}}^{r},
                                       \bar{w}_{i+1/2,i+2}^{e}, \partial_{x}w_{i+1/2,j_{i}}^{e}, \partial_{xx}w_{i+1/2,j_{i}}^{e}, \partial_{y}w_{i+1/2,j_{i}}^{e}, \partial_{yy}w_{i+1/2,j_{i}}^{e}, \partial_{yy}w_{i+1/2,j_{i}}^{e},
   1 foreach cell \Omega_{ij} do
                      // as an example, interface (i+1/2,j) left side reconstruction is
                                  shown.
                      // normal reconstruction
                     if x-direction then
   2
                                 using 5th order reconstruction(WENO5-Z or TENO5);
   3
                                 calculate (\hat{w}_{i+1/2,i}^l, (\hat{w}_x)_{i+1/2,j}^l) \leftarrow (\bar{w}_{i-2,j}, \bar{w}_{i-1,j}, \bar{w}_{i,j}, \bar{w}_{i+1,j}, \bar{w}_{i+2,j})
    4
                      end
   5
                     if y-direction then
   6
                       similar to x-direction
   7
                      end
   8
                      // tangential reconstruction
                     if x-direction then
   9
                                 foreach Gaussian point \mathbf{x}_m at the interface (i+1/2,j) do
 10
                                             // here the index i+1/2 is omitted
                                             using 5th order reconstruction(WENO5-Z or TENO5);
 11
                                            calculate (w_{i,m}^l, (w_x)_{i,m}^l, (w_y)_{i,m}^l) \leftarrow (\hat{w}_{i-2}^l, \hat{w}_{i-1}^l, \hat{w}_{i}^l, \hat{w}_{i+1}^l, \hat{w}_{i+2}^l, (\hat{w}_x)_{i}^l)
 12
                                 end
 13
                      end
 14
                     if y-direction then
15
                         similar to x-direction
 16
                     end
 17
18 end
          // similar to interface (i+1/2,j) right side reconstruction.
19 foreach interface do
                      calculate interface equilibrium state values and first-order derivatives by
                         Eq. (4.13) (w_{i+1/2,i}^e, (w_x)_{i+1/2,i}^e) \leftarrow (w_{i+1/2,i}^{l,r}, (w_x)_{i+1/2,i}^{l,r}),
                      foreach Gaussian point \mathbf{x}_m at the interface (i+1/2,j) do
21
                        calculate (w_{j,m}^e, (w_x)_{j,m}^e, (w_y)_{j,m}^e);
 22
                     end
 23
24 end
25 return
```

## 4.3 Two-stage fourth-order temporal discretization

In this section, a two-stage fourth-order gas-kinetic scheme is presented based on the time-dependent gas distribution function (4.14) at each cell interface.

Consider the following time-dependent equation,

$$\frac{\partial w}{\partial t} = \mathbf{L}(w),\tag{4.20}$$

with the initial condition at  $w(t=t_n)=w^n$ , where L is an operator for the spatial derivative of flux. The time derivatives are obtained

$$\frac{\partial w^n}{\partial t} = \mathbf{L}(w^n), \quad \frac{\partial}{\partial t} \mathbf{L}(w^n) = \frac{\partial}{\partial w} \mathbf{L}(w^n) \mathbf{L}(w^n). \tag{4.21}$$

Introducing an intermediate state at  $t^* = t_n + \Delta t/2$ ,

$$w^* = w^n + \frac{1}{2}\Delta t \mathbf{L}(w^n) + \frac{1}{8}\Delta t^2 \frac{\partial}{\partial t} \mathbf{L}(w^n), \tag{4.22}$$

with a third-order accuracy. the corresponding time derivatives are obtained as well for the intermediate state,

$$\frac{\partial w^*}{\partial t} = \mathbf{L}(w^*), \quad \frac{\partial}{\partial t} \mathbf{L}(w^*) = \frac{\partial}{\partial w} \mathbf{L}(w^*) \mathbf{L}(w^*). \tag{4.23}$$

Then, the state w can be updated with the following formula,

$$w^{n+1} = w^n + \Delta t \mathbf{L}(w^n) + \frac{1}{6} \Delta t^2 \left( \frac{\partial}{\partial t} \mathbf{L}(w^n) + 2 \frac{\partial}{\partial t} \mathbf{L}(w^*) \right). \tag{4.24}$$

For the hyperbolic equation, the above time stepping method provides a fourth-order time accurate solution for w(t) at  $t = t_n + \Delta t$ . We apply this approach to conservation laws

$$w^{n+1} = w^n + \Delta t \mathbf{L}(w^n) + \frac{1}{6} \Delta t^2 \left( \frac{\partial}{\partial t} \mathbf{L}(w^n) + 2 \frac{\partial}{\partial t} \mathbf{L}(w^*) \right), \tag{4.25}$$

where w is a conservative variable and f(w) is the corresponding flux,

$$\frac{\partial w_i}{\partial t} = \mathbf{L}_i(w) = -\frac{1}{\Delta x_i} (f_{i+1/2} - f_{i-1/2}).$$
 (4.26)

For the gas-kinetic scheme, the corresponding flux is a complicated function of time. To obtain the time derivatives of the flux function at  $t_n$  and  $t_* = t_n + \Delta t/2$ , the flux function should be approximated as a linear function of time within a time interval

$$\mathcal{F}_{i+1/2}(W^n,\delta) = \int_{t_n}^{t_n+\delta} F_{i+1/2}(W^n,t) \, \mathbf{d}t = \int_{t_n}^{t_n+\delta} \int u \psi f(x_i+1/2,t,u,v,\xi) dE dt. \tag{4.27}$$

In the time interval  $[t_n, t_n + \Delta t]$ , the flux is expanded as the following linear form

$$F_{i+1/2}(W^n, t) = F_{i+1/2}^n + (t - t_n) \partial_t F_{i+1/2}^n, \tag{4.28}$$

the coefficients  $F_{i+1/2}^n$  and  $\partial_t F_{i+1/2}^n$  can be determined as follows,

$$F_{i+1/2}(W^n, t_n)\Delta t + \frac{1}{2}\partial t F_{i+1/2}(W^n, t_n)\Delta t^2 = \mathcal{F}_{i+1/2}(W^n, \Delta t), \tag{4.29}$$

$$\frac{1}{2}F_{i+1/2}(W^n, t_n)\Delta t + \frac{1}{8}\partial t F_{i+1/2}(W^n, t_n)\Delta t^2 = \mathcal{F}_{i+1/2}(W^n, \Delta t/2). \tag{4.30}$$

By solving the linear system, we have

$$F_{i+1/2}(W^n, t_n) = (4\mathcal{F}_{i+1/2}(W^n, \Delta t/2) - \mathcal{F}_{i+1/2}(W^n, \Delta t)) / \Delta t, \tag{4.31}$$

$$\partial_t F_{i+1/2}(W^n, t_n) = 4(\mathcal{F}_{i+1/2}(W^n, \Delta t) - 2\mathcal{F}_{i+1/2}(W^n, \Delta t/2))/\Delta t^2. \tag{4.32}$$

Similarly,  $F_{i+1/2}(W^*,t^*)$ ,  $\partial_t F_{i+1/2}(W^*,t^*)$  for the intermediate state can be constructed.

With these notations, the two-stage algorithm for both the Euler and Navier-Stokes equations is given as follows

(i) With the initial reconstruction, update  $W^*$  at  $t_* = t_n + \Delta t/2$  by

$$W^* = W^n - \frac{1}{\Delta x} [\mathcal{F}_{i+1/2}(W^n, \Delta t/2) - \mathcal{F}_{i-1/2}(W^n, \Delta t/2)], \tag{4.33}$$

and compute the fluxes and their derivatives,

$$F_{i+1/2}(W^n, t_n), \partial_t F_{i+1/2}(W^n, t_n).$$
 (4.34)

(ii) Reconstruct intermediate value W\*, and compute

$$F_{i+1/2}(W^*, t_*), \partial_t F_{i+1/2}(W^*, t_*),$$
 (4.35)

where the derivatives are dertermined in the time interval  $[t_*, t_* + \Delta t]$ .

(iii) Update  $W^{n+1}$  by

$$W^{n+1} = W^n - \frac{1}{\Lambda x} [\mathcal{F}_{i+1/2}(W^n, \Delta t) - \mathcal{F}_{i-1/2}(W^n, \Delta t)], \tag{4.36}$$

where  $\mathcal{F}_{i+1/2}(W^n, \Delta t)$  are expressed as,

$$\mathcal{F}_{i+1/2}(W^n, \Delta t) = \Delta t F_{i+1/2}(W^n, t_n) + \frac{1}{6} \Delta t^2 (\partial_t F_{i+1/2}(W^n, t_n) + 2\partial_t F_{i+1/2}(W^*, t_*)). \tag{4.37}$$

In summary, based on the distribution function for the flux in the smooth region, the above scheme solves the Euler or Navier-Stokes equations with the leading-order error of  $\mathcal{O}((\Delta x)^5,(\Delta t)^4)$ . Finally, a summary of the solution procedure for GKS is given in Fig. 2

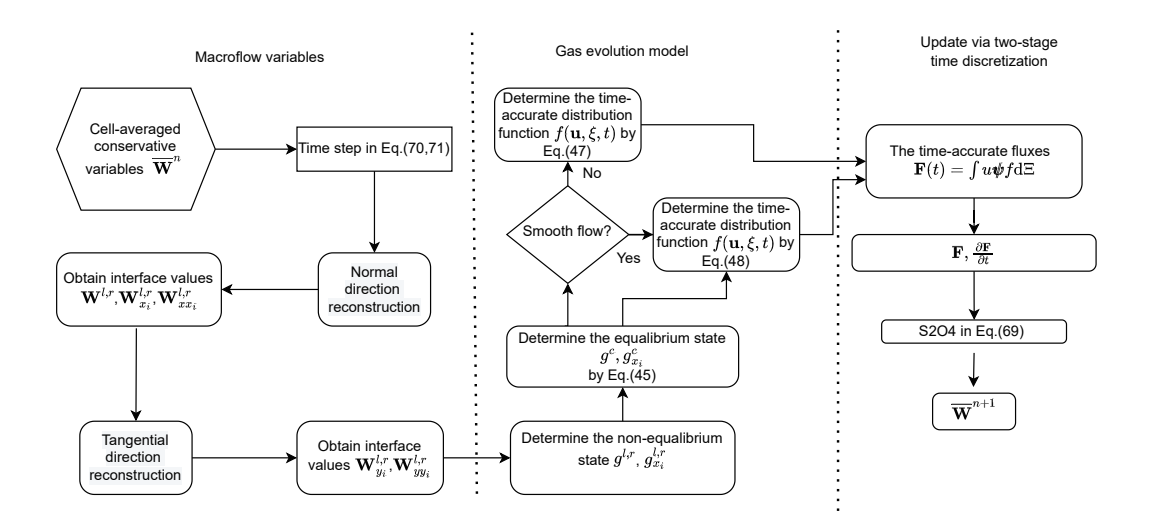


Figure 2: The brief algorithm of the high-order GKS.

## 5 Numerical results

In the following test cases of the inviscid flows, the time step is determined by

$$\Delta t = \text{CFL} \times \frac{\Delta x}{(|\mathbf{U}| + C)_{\text{Max}}},\tag{5.1}$$

where *C* is sound speed. For the viscous flow, the time step is determined by,

$$\Delta t = \text{CFL} \times \text{Min} \left[ \frac{\Delta x}{(|\mathbf{U}| + C)_{\text{Max}}}, \frac{\rho \Delta x^2}{4\mu} \right]. \tag{5.2}$$

## 5.1 1-D tests

## 5.1.1 Accuracy test in 1D

The first case concerns the advection of density perturbations, the initial condition is set as follows

$$\rho(x) = 1 + 0.2\sin(\pi x), \quad U(x) = 1, \quad p(x) = 1, \quad x \in [0,2].$$

The boundary condition is a periodic boundary condition, and the analytic solution is

$$\rho(x,t) = 1 + 0.2\sin(\pi(x-t)), \quad U(x) = 1, \quad p(x) = 1.$$

In the computation, a uniform mesh with N points is used. In this test, a fixed CFL number CFL = 0.1 is used for different meshes. With the fifth-order spatial reconstruction, the leading-order truncation error in the inviscid case from the fourth-order GKS is

Mesh length	L1 error	L1 order	L2 error	L2 order
1/20	2.558609e-05		2.845558e-05	
1/40	8.406174e-07	4.93	9.344976e-07	4.93
1/80	2.980860e-08	4.82	3.319259e-08	4.82
1/160	1.273925e-09	4.55	1.418256e-09	4.55
1/320	6.709996e-11	4.25	7.461086e-11	4.25
1/640	3.945189e-12	4.09	4.383633e-12	4.09

Table 1: TENO5 S2O4.

 $\mathcal{O}(\Delta x^5 + \Delta t^4)$ . With the fixed CFL number, we have  $\Delta t = c\Delta x$  and the leading term becomes  $\mathcal{O}(\Delta x^5 + \Delta t^4) \sim \mathcal{O}(\Delta x^5 + c^4 \Delta t^4)$ . With the mesh refinement, the order of accuracy will converge to 4. The L1 and L2 errors and orders at t=2 are presented in Table 1. The expected order accuracy can be achieved.

#### 5.1.2 The Titarev and Toro problem

The Titarev and Toro problem considers the propagation of high-frequency oscillating sinusoidal wave with the presence of a shock, which is a great challenge for spatial reconstruction and flux solver [27,28]. This problem consists of a right-facing shock wave impinging on a high-frequency density perturbation, a challenging problem for the flux solver and reconstruction. The initial condition for the Toro problem is given by

$$(\rho, U, p) = \begin{cases} (1.515695, 0.523346, 1.805), & 0 < x < 0.5, \\ ((1+0.1\sin(20\pi x)), 0.1), & 0.5 < x < 10. \end{cases}$$
(5.3)

The computational domain is [0,10] with 1000 cells. The computed density profiles and local enlargements for the Toro problem at t=5 with both the reconstruction scheme are plotted in Fig. 3. The results are also compared with the HLLC and LF solver. As shown in Fig. 4, at the entropy wave part, the GKS scheme resolves the density fluctuations better than the HLLC and LF solvers. Meanwhile, by changing reconstruction to TENO, TENO-LF, and TENO-HLLC solvers perform better than WENO-LF and WENO-HLLC, while the GKS results are not sensitive to the reconstruction method.

## 5.1.3 The blast wave problem

The initial condition for the Woodward-Colella blast wave problem [33] is given by

$$(\rho, U, p) = \begin{cases} (1,0,1000), & 0 < x < 0.1, \\ (1,0,0.01), & 0.1 < x < 0.9, \\ (1,0,100), & 0.9 \le x < 1. \end{cases}$$
 (5.4)

A reflective boundary condition is imposed at x = 0 and x = 1. The simulation is performed on a uniform mesh with N = 400 with CFL = 0.5. Fig. 5 displays the computed profiles of density at t = 0.038. The blast wave problem requires the robustness and the

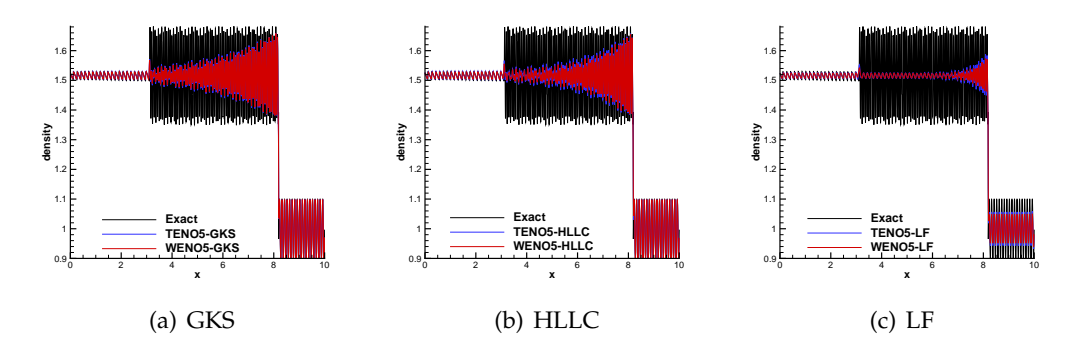


Figure 3: Titarev-Toro problem by (a) GKS, (b) HLLC, and (c) LF schemes. Density distribution with 1000 mesh points and t = 5.0. The CFL number is 0.5.

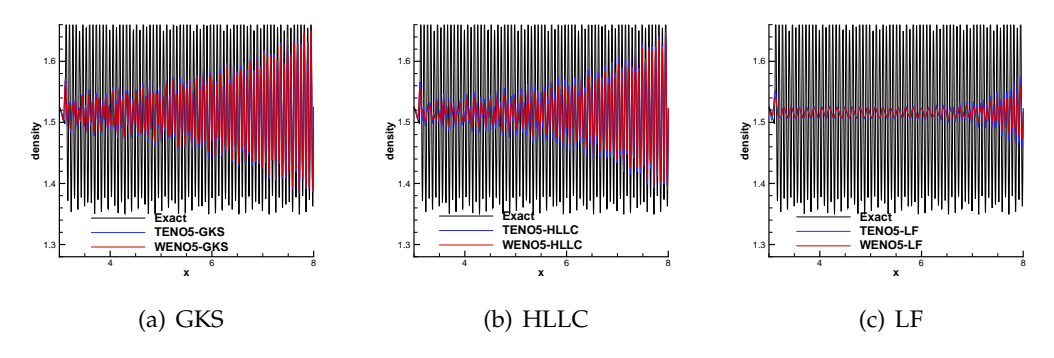


Figure 4: enlarge the domain of (a) GKS, (b) HLLC, and (c) LF at t = 5.0.

ability of strong shock capturing. To show the potential of GKS. The fifth-order WENO5 reconstruction with GKS is compared with the eighth-order reconstruction TENO8 with LF. TENO8-LF can only result when  $C_T = 10^{-4}$ . WENO5-GKS resolves the density profile better than TEN8-LF near the right peak x = 0.78. Hence, we can conclude that using a higher-order flux solver should be a better choice compared to higher-order reconstruction.

#### **5.2 2-D** tests

## 5.2.1 Interaction of planar shocks

In the following two-dimensional Riemann problems, two classic examples are considered [17] The computation domain is  $[0,1] \times [0,1]$  covered by  $400 \times 400$  uniform mesh points, where the non-reflecting boundary conditions are used in all boundaries. The

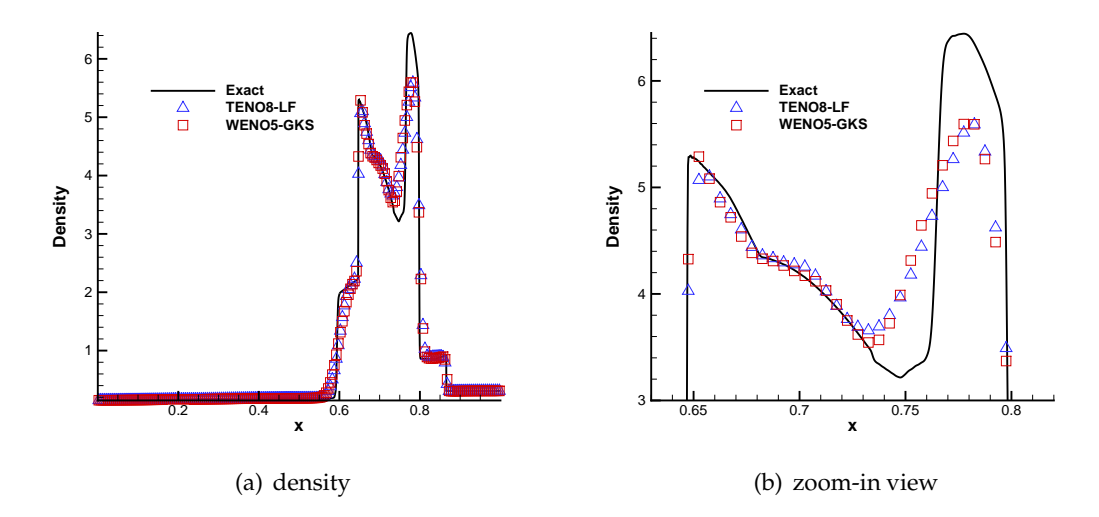


Figure 5: The density distributions for blast wave problem at t = 0.038 with 200 cells, CFL = 0.5.

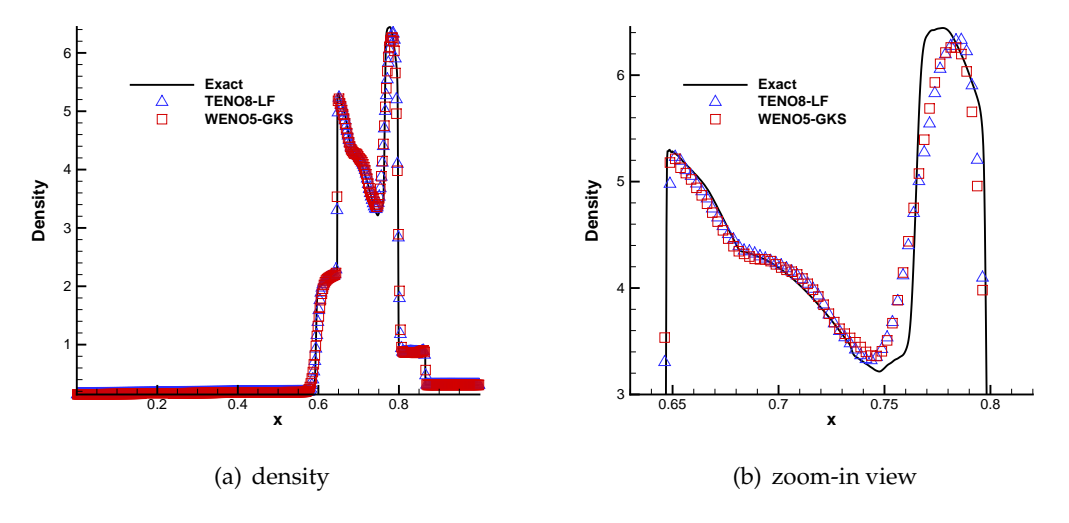


Figure 6: The density distributions for blast wave problem at t = 0.038 with 400 cells, CFL = 0.5.

initial condition for the first problem is given by

$$(\rho, U, V, p) = \begin{cases} (0.138, 1.206, 1.206, 0.029), & x < 0.7, & y < 0.7, \\ (0.5323, 0, 1.206, 0.3), & x \ge 0.7, & y < 0.7, \\ (1.5, 0, 0, 1.5), & x \ge 0.7, & y \ge 0.7, \\ (0.5323, 1.206, 0, 0.3), & x < 0.7, & y \ge 0.7. \end{cases}$$
(5.5)

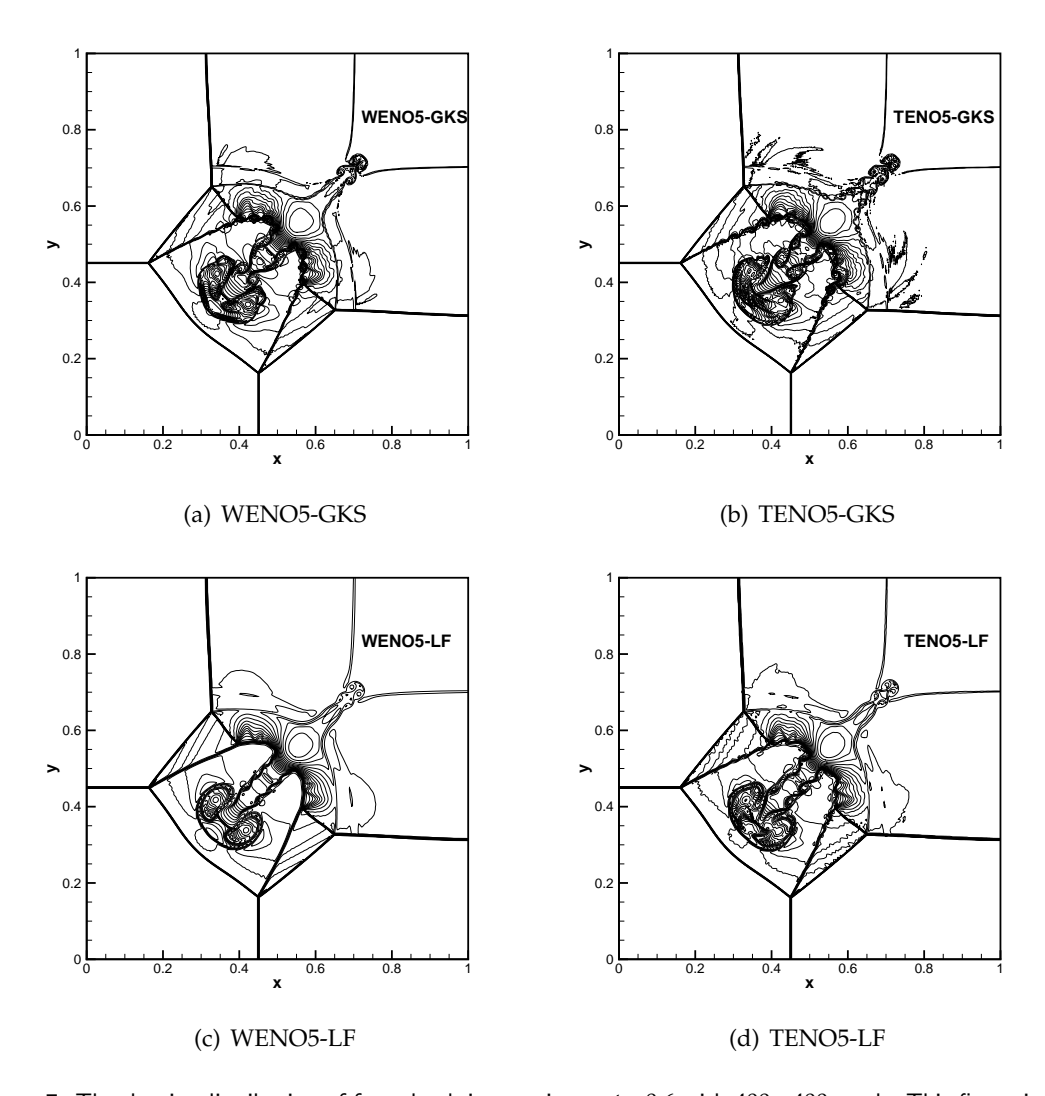


Figure 7: The density distribution of four shock-interaction at  $t\!=\!0.6$  with  $400\!\times\!400$  mesh. This figure is drawn with 32 density contours between 0.16 and 1.71.

The density distribution simulated by WENO5-GKS, TENO5-GKS, WENO5-LF, and TENO5-LF are presented at  $t\!=\!0.6$  in Fig. 12(d). The four schemes can resolve small-scale flow structures. The low-dissipation TENO reconstruction can better resolve smaller structures compared to WENO5. However, the solution of TENO5-GKS and TENO5-LF violates the flow symmetry severely while WENO5-GKS and WENO5-LF preserve it well. This kind of symmetry breaking not only appeared in TENO reconstruction but also in some high-order low-dissipative reconstructions such as WENO9-JS and can be solved by reordering the multiplication in simulation code [32]. Fleischmann et al. [6] also demonstrate that symmetry breaking is induced by the floating-point truncation errors that grow exponentially with long-term evolution instead of instabilities.

## 5.2.2 Interaction of planar contact discontinuities

The initial condition for the second 2-D Riemann problem is given by

$$(\rho, U, V, p) = \begin{cases} (1, -0.75, 0.5, 1), & x < 1, \quad y < 1, \\ (3, -0.75, -0.5, 1), & x \ge 1, \quad y < 1, \\ (1, 0.75, -0.5, 1), & x \ge 1, \quad y \ge 1, \\ (2, 0.75, 0.5, 1), & x < 1, \quad y \ge 1, \end{cases}$$
(5.6)

where four zones have the same pressure but different density and velocity. Four shear layers will be formed by planar contact discontinuity interactions. The computation domain is  $[0,2] \times [0,2]$  covered by  $800 \times 800$  uniform mesh points. The CFL condition is 0.5 in all calculations. This case is to simulate the shear instabilities among four initial contact discontinuities. The density distribution simulated by WENO5-GKS, TENO5-GKS, WENO5-LF, and TENO5-LF are presented at the t=0.4 and t=1.6 in Fig. 8.

The discontinuities in the 2D Riemann problem cause the Kelvin-Helmholtz instabilities due to the numerical viscosities. It is generally believed that smaller numerical dissipation accords with larger amplitude shear instabilities. As shown in Fig. 8, at t=0.4, the results for TENO-GKS and WENO-GKS show more small vortices than TENO-LF and WENO-LF. At time t=1.6, the flow structure becomes much more complicated and WENO-GKS and WENO-LF show more dissipative results than TENO-GKS and TENO-LF. In both TENO5-GKS and TENO5-LF, the high-order accuracy of the initial non-equilibrium state by the TENO5 reconstruction helps reduce numerical dissipation and leads to better overall results.

#### 5.2.3 The Noh Problem in 2D

The 2-D Noh problem is an implosion test to model the gas compression with constant radial velocity towards a circle center, where a moving strong shock wave is formed [22]. The computational domain is  $[0,1]^2$ . The initial density and pressure are  $\rho=1$  and  $p=1\times 10^{-4}$ , and the velocity is  $(u,v)=(-x,-y)/\sqrt{x^2+y^2}$ . The ratio of the specific heat is  $\gamma=5/3$ . The inviscid wall condition is adopted along the boundaries x=0 and y=0. The supersonic inflow boundary condition is imposed on the other boundaries with the same pressure and velocity as the initial conditions. The analytical solution of density is

$$(\rho, U, V, p) = \begin{cases} 16, -x/\sqrt{x^2 + y^2}, -y/\sqrt{x^2 + y^2}, 10^{-4}, & r < t/3, \\ 1 + t/r, (-x)/\sqrt{x^2 + y^2}, (-y)/\sqrt{x^2 + y^2}, 10^{-4}, & r > t/3. \end{cases}$$
(5.7)

The results of the WENO5 reconstruction with GKS solver and LF on the  $400 \times 400$  grids with CFL = 0.5 are shown in Fig. 9 and Fig. 10. In this case, WENO5-GKS can simulate the 2-D Noh test, while WENO5-LF failed in the first time step, but can evolve that by decreasing the initial pressure to  $p = 1 \times 10^{-3}$ . In WENO5 construction, the accuracy of the WENO5-GKS for strong shock waves is verified by the precise post-shock density solution which is higher than the result of WENO5-LF. TENO5-GKS and TENO5-LF in this case failed to run while they blew up after a few time steps.

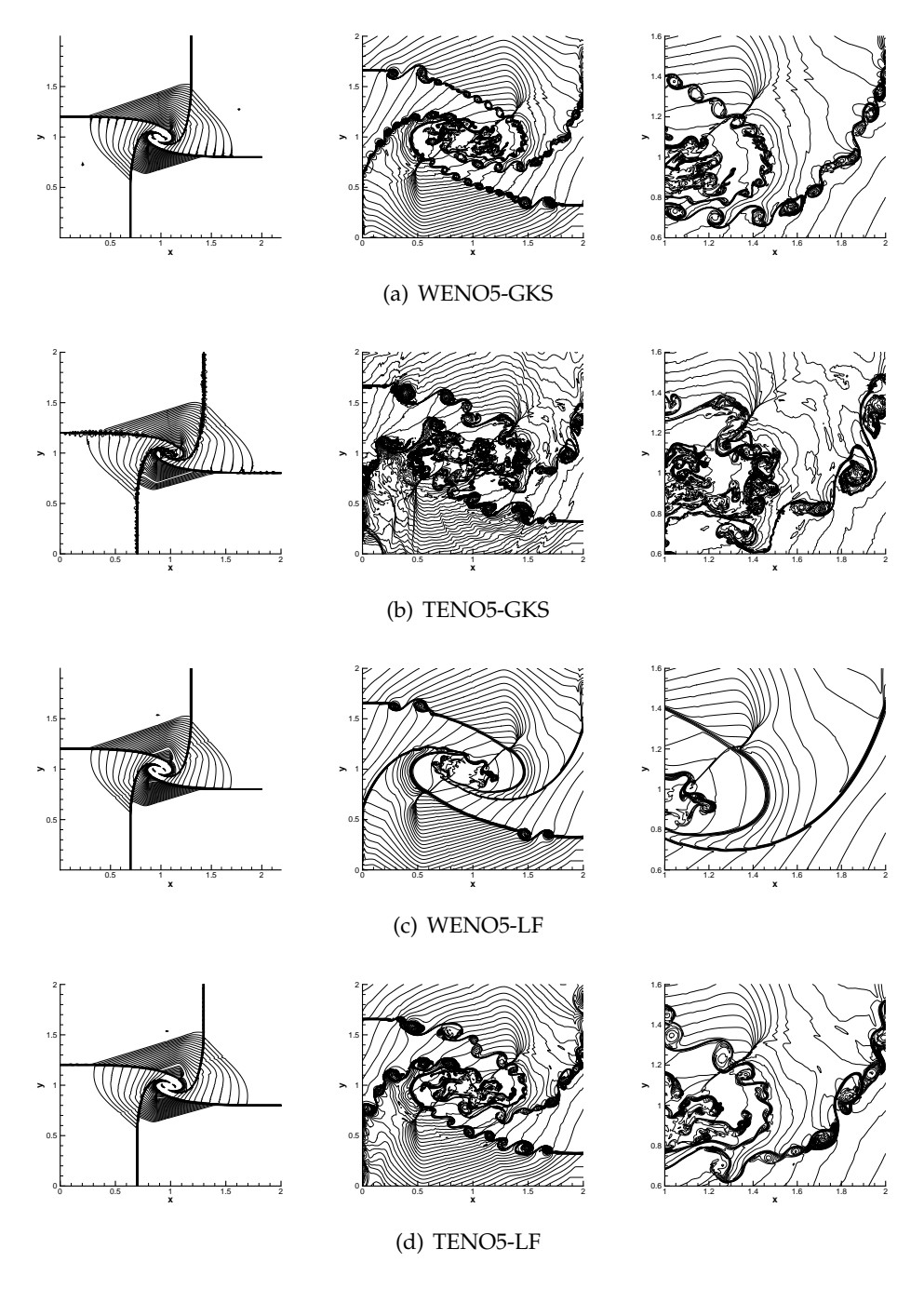


Figure 8: 40 equal-spaced density contours of planar contact discontinuities. Left: t=0.4. Middle: t=1.6. Right: local enlargement of t=1.6.  $800\times800$  grids are used.

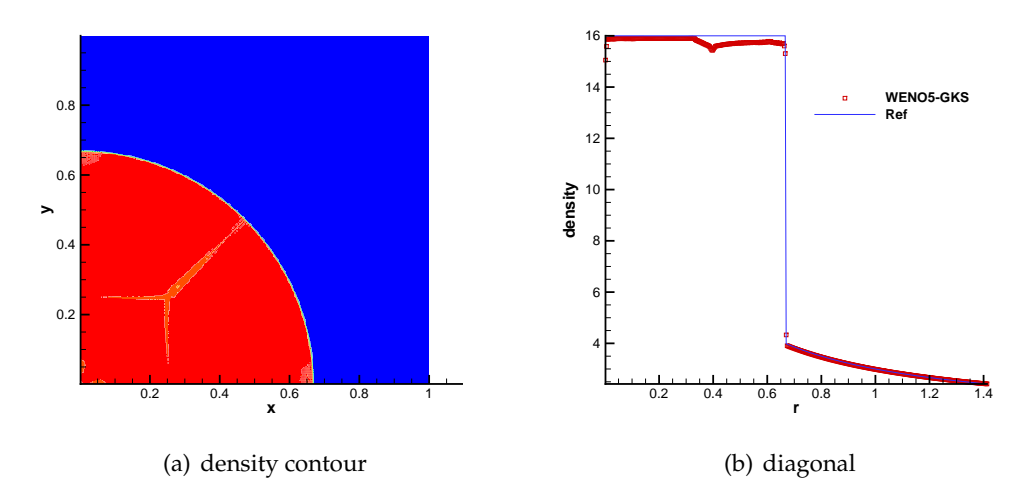


Figure 9: Noh problem with WENO5-GKS solver at time =2.0. Resolution at  $400 \times 400$ .

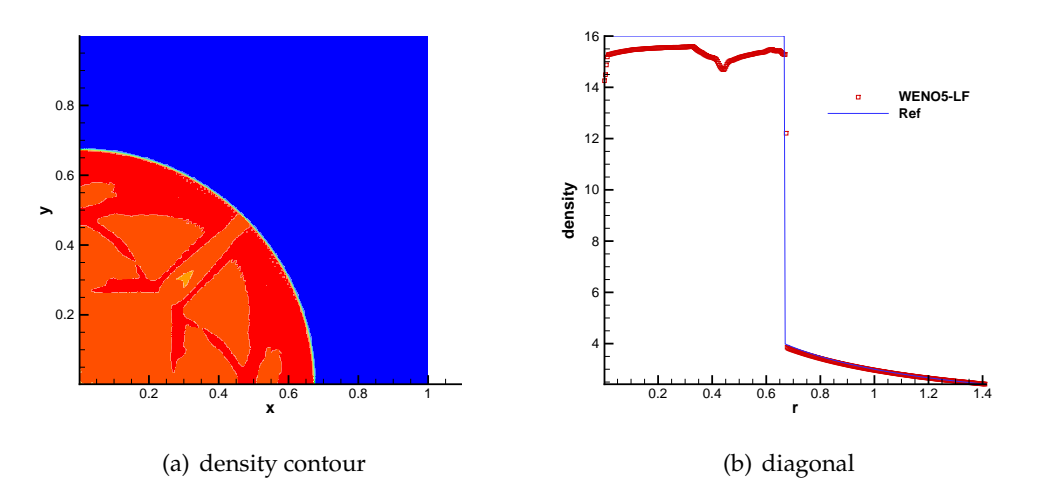


Figure 10: Noh problem with WENO5-LF solver at time =2.0. Resolution at  $400\times400$ .

## 5.2.4 Double Mach reflection problem

This problem is studied for inviscid flow [33]. The computational domain is  $[0,4] \times [0,1]$ , and a solid wall lies at the bottom of the computational domain starting from x = 1/6. Initially, a right-moving Mach 10 shock is positioned at (x,y) = (1/6,0), and makes a  $60^{\circ}$  angle with the x-axis. The initial pre-shock and post-shock conditions are

$$(\rho, U, V, p) = \begin{cases} (8, 4.125\sqrt{3}, -4.125, 116.6), \\ (1.4, 0, 0, 1). \end{cases}$$
 (5.8)

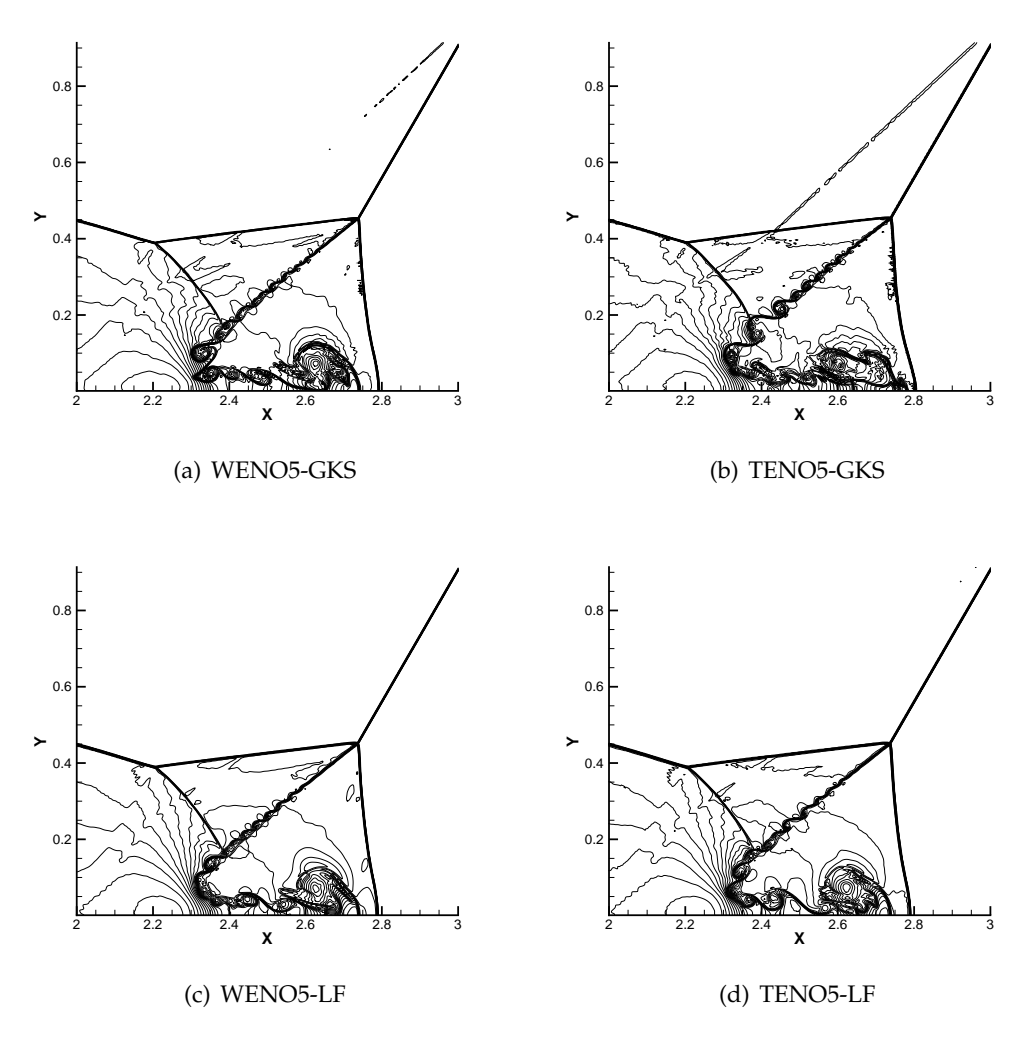


Figure 11: Double Mach reflection of a strong shock: density contours at simulation time t = 0.2. Resolution at  $1920 \times 480$ . This figure is drawn with 43 density contours between 1.887 and 20.9.

The reflecting boundary condition is used at the wall. For the rest of the bottom boundary, the exact post-shock condition is imposed. At the top boundary. The density distributions with  $1920 \times 480$  uniform mesh points at t = 0.2 with WENO and TENO are shown below.

In this case, all four schemes show good robustness and can capture the flow structure well. The double Mach reflection problem demonstrates the good robustness of all four schemes. From the local enlargement, The WENO5-GKS scheme and TENO5-GKS scheme resolve the contact and shock waves much sharper than the standard WENO5-LF scheme and TENO5-LF scheme, leading to a substantially improved prediction of the shear-layer instabilities.

## 5.2.5 Viscous shock tube problem

Next, the viscous shock tube problem was introduced to test the performance of different schemes for viscous flows. It is a shock tube problem in a 2-D square box  $[0,1] \times [0.1]$ , and the diaphragm is located at x = 0.5. The initial state is given as follows:

$$(\rho, U, V, p) = \begin{cases} (120, 0, 0, 120/\gamma), & 0 < x < 0.5, \\ (1.2, 0, 0, 1.2/\gamma), & 0.5 \le x < 1, \end{cases}$$
(5.9)

where  $\gamma=1.4$  and Prandtl number Pr=0.73. The simulation at Re=200 is tested. The output time is t=1.0. For the boundary condition, the upper boundary is asymmetric boundary, and others are the non-slip adiabatic walls. The density contour is shown in Fig. 12, where all four schemes can capture the main flow structures. The  $\lambda$ -shape structure, the vortices within the boundary layer, and the slip line in the lower right region are captured clearly. The density profiles along the bottom wall are shown in Fig. 13 with the local enlargement. The results show that both schemes have similar resolution, while WENO5-GKS is slightly better.

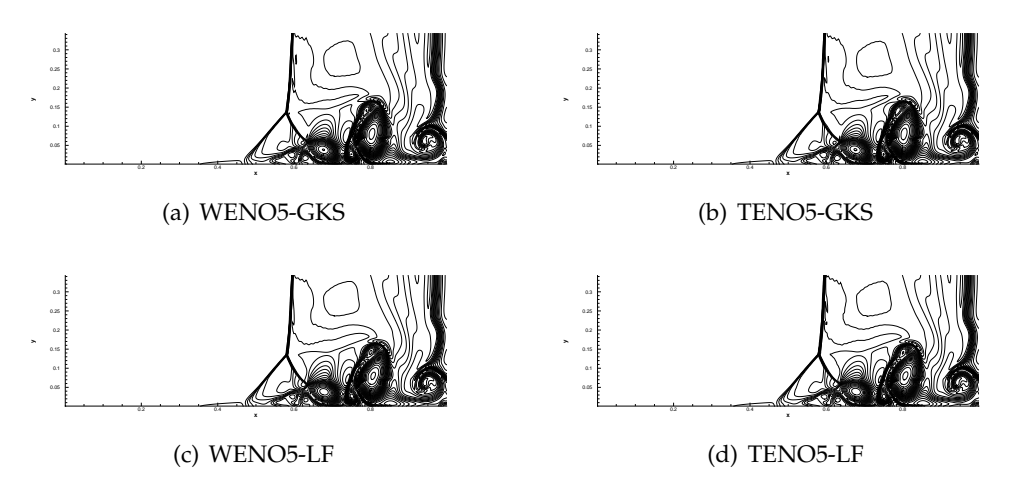


Figure 12: Viscous shock tube problem with Re =200: density contours at simulation time t=1. Resolution at  $500\times250$ . This figure is drawn with 30 density contours between 20 and 130.

#### 5.3 3-D tests

## 5.3.1 Taylor-Green vortex

The three-dimensional Taylor-Green vortex is simulated by WENO5-GKS, WENO5-HLLC, TENO5-GKS, and TENO5-HLLC. The computational domain is  $[-\pi L, \pi L] \times$ 

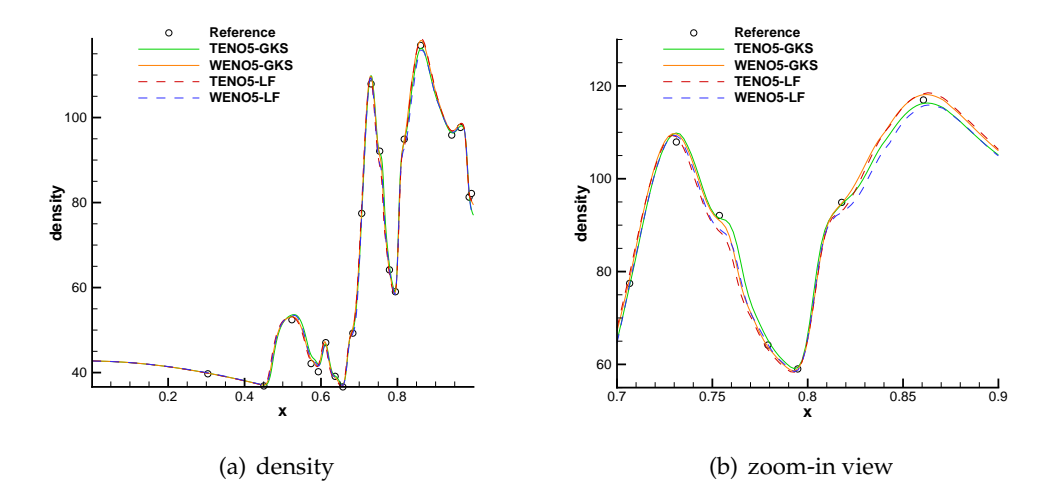


Figure 13: Viscous shock tube problem of Re = 200: density profile along the bottom wall (y=0). The right is the enlarged figure. For all cases, the CFL number is 0.2.

$$[-\pi L, \pi L] \times [-\pi L, \pi L]$$
, and the initial condition is  $U = U_0 \sin(x/L) \cos(y/L) \cos(z/L)$ ,  $V = -U_0 \cos(x/L) \sin(y/L) \cos(z/L)$ ,  $W = 0$ ,  $p = p_0 + \rho_0 U_0^2 (\cos(2x/L) + \cos(2y/L)) (\cos(2z/L) + 2)/16$ .

The parameters are set as L=1,  $U_0=1$ ,  $\rho_0=1$ . The Mach number is  $Ma=U_0/C=0.1$ , and the sound speed is  $C=\sqrt{\gamma RT}$ . The mesh numbers are  $64^3$  and  $128^3$ , and periodic boundary condition is imposed at all boundaries. The volume-averaged kinetic energy is defined as,

$$E_k = \frac{1}{\rho_0 \Omega} \int_{\Omega} \frac{\rho \left( U^2 + V^2 + W^2 \right)}{2} d\Omega,$$

where  $\Omega$  is the total volume of the flow field. The dissipation rate of the kinetic energy is given by

$$\epsilon_k = -\frac{\mathrm{d}E_k}{\mathrm{d}t}.$$

The linear reconstruction is taken for both schemes in this test case. The Reynolds number is defined as  $Re=U_0L/\nu$ , and two Reynolds numbers, Re=280 and Re=1600, are calculated by four schemes. The results of Re=280 with mesh number  $64^3$  are presented in Fig. 14, and compared with a reference solution generated with spectral method [31]. The CFL number is 0.5 for WENO5-GKS and TENO5-GKS while 0.3 for WENO5-HLLC and TENO5-HLLC. If the CFL number is 0.4, The HLLC generates a large oscillation. The reason might be that the HLLC flux is constructed by the normal direction reconstruction while for GKS flux is intrinsically multi-dimensional which also considers the

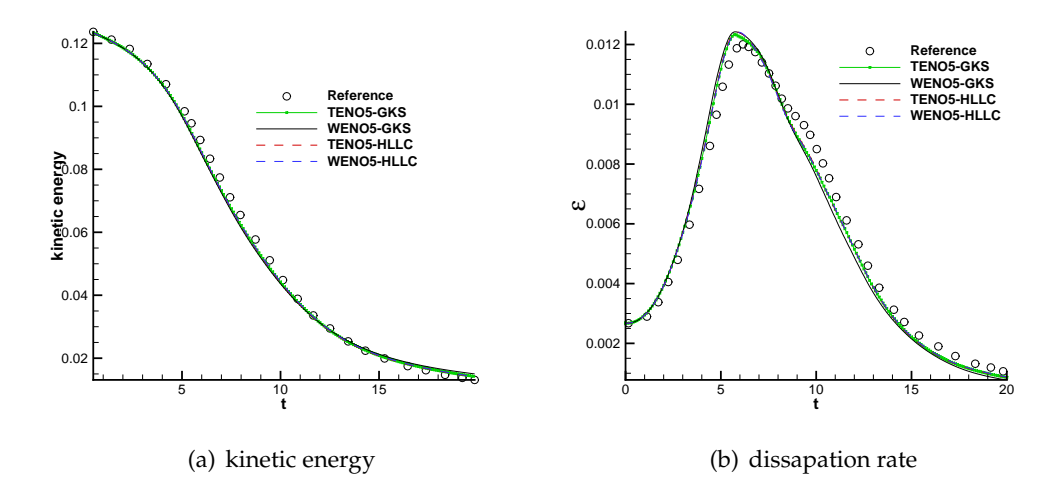


Figure 14: Taylor-Green vortex problem with Re = 280 by WENO5-GKS, WENO5-HLLC, TENO5-GKS, and TENO5-HLLC schemes: the kinetic energy (left) and the dissipation rate (right). The CFL number is 0.5 for the GKS scheme and 0.3 for the HLLC scheme. For both cases, the mesh number is  $64^3$ .

tangential gradients. The multi-dimensional structure of the Taylor-Green vortex might be more consistent with the GKS flux. To improve the robustness of WENO5-HLLC abd TENO5-HLLC scheme, the conservative variables at the cell interface  $Q_{i+1/2}$  are obtained by simple averaging of the left and right interface values of reconstruction. Although changing reconstruction from WENO to TENO cannot be run at higher CFL number results for HLLC, TENO-GKS shows a better solution than WENO-GKS in dissipation rate in Fig. 14(b). Furthermore, for higher Reynolds numbers, results for Re = 1600 with mesh number  $128^3$  are shown in Fig. 15. The reference for Re = 1600 is also generated with spectral method from [5], and a similar conclusion can be obtained with Re = 280.

For Re = 280, the integrated enstrophy is also considered, which is defined as

$$\zeta = \frac{1}{\rho_0 \Omega} \int_{\Omega} \frac{1}{2} \rho |\nabla \times \mathbf{U}|^2 d\Omega,$$

where  $\zeta$  is calculated by the central difference method. The reference solution is from DeBonis [5].

For the enstrophy  $\zeta$ , the result of the TENO5-HLLC scheme is obviously better than the WENO5-HLLC scheme, while there is only a tiny difference between TENO5-GKS and WENO5-GKS. Both TENO5-GKS and WENO5-GKS results yield almost converged (i.e., grid-independent) results when compared to the reference data. This contrast further highlights the relative insensitivity of GKS flux solver to the reconstruction methodology.

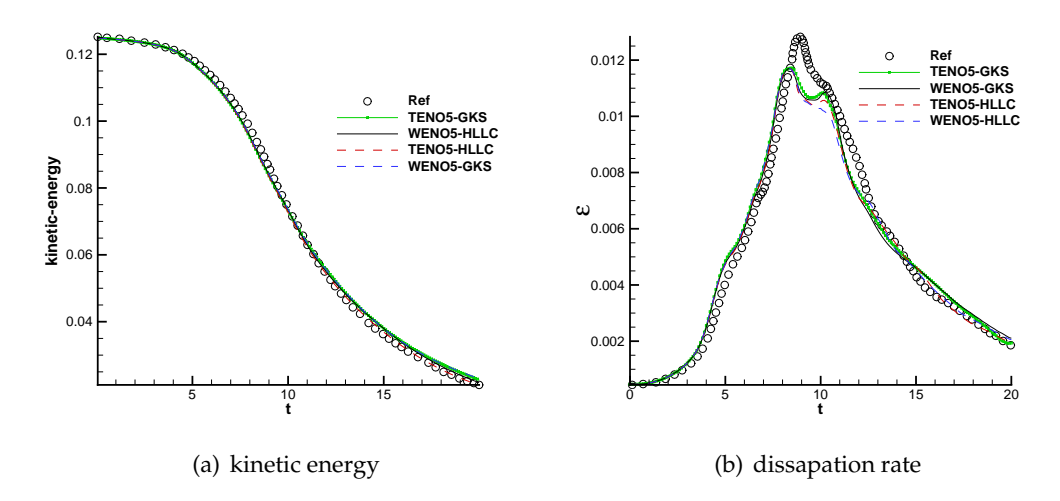


Figure 15: Taylor-Green vortex problem with Re = 1600 by WENO5-GKS, WENO5-HLLC, TENO5-GKS, and TENO5-HLLC schemes: the kinetic energy (left) and the dissipation rate (right). The CFL number is 0.5 for the GKS scheme and 0.3 for the HLLC scheme. For both cases, the mesh number is  $128^3$ .

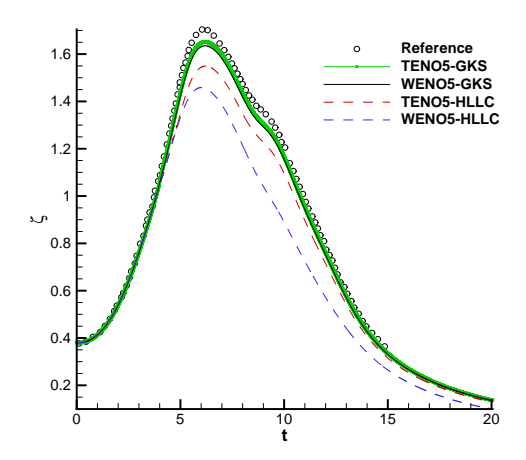


Figure 16: Taylor-Green vortex problem with Re = 280 by WENO5-GKS, WENO5-HLLC, TENO5-GKS, and TENO5-HLLC schemes: the enstrophy. The CFL number is 0.5 for the GKS scheme and 0.3 for the HLLC scheme. For both cases, the mesh number is  $128^3$ .

# 6 Computational efficiency

The computational efficiencies of WENO5-GKS, WENO5-HLLC, TENO5-GKS, and TENO5-HLLC are compared in 2-D and 3-D cases. The computational time mainly includes reconstruction and flux construction. For the reconstruction, WENO5-HLLC and TENO5-HLLC need only pointwise conservative values, while the derivative is also

Table 2: 2-D computational efficiency test of shock-interaction problem. The mesh number is  $400 \times 400$ . The shown CPU time is obtained for 10 time steps by a single Intel core i7-8750 @ 2.20GHz.

	CPU time(s)	Time ratio
WENO5-GKS	133.74	1.00
WENO5-HLLC	216.41	1.62
TENO5-GKS	135.11	1.01
TENO5-HLLC	218.02	1.63

Table 3: 3-D computational efficiency test of Taylor-Green vortex problem with  $Ma_t = 0.1$  and CFL = 0.3. The mesh number is  $64^3$ . The shown CPU time is obtained for 10 time steps by a single Intel core i7-8750 @ 2.20GHz.

	CPU time(s)	Time ratio
WENO5-GKS	506.35	1.00
WENO5-HLLC	789.62	1.56
TENO5-GKS	508.46	1.01
TENO5-HLLC	791.80	1.57

needed in WENO5-GKS and TENO5-GKS. Compared to WENO reconstruction, TENO has an extra step for scale separation. For the flux construction, the GKS is more complicated than HLLC, but GKS uses two stages instead of four stages in HLLC to achieve 4th-order time accuracy.

The shock-interaction problem is used to test the computational efficiency. The mesh in this test is  $400 \times 400$ . In this case, the computation time and relative efficiency are listed in Table 2 The computation time is shown in Table 2 are obtained for 10 time steps by a single Intel core i7-8750 @ 2.20GHz. The results show that WENO5-HLLC is 62% more expensive than WENO5-GKS in the 2-D shock-interaction problem, while TENO5-GKS consumes almost the same time compared to WENO5-GKS. The next test is the Taylor-Green vortex in 3-D. Again, the computational time is collected by running the program for 10 time steps, and the results are shown in Table 3. The computational time of WENO5-HLLC is 56% slower than WENO5-GKS. Changing to TENO reconstruction slightly increases the computational time. This is mainly due to the temporal discretization. More time stages in one time step will increase the computational time.

## 7 Discussions

In the latest TENO reconstruction, the basic idea is to judge whether the solution in a stencil is smooth or not by the scale separation. The TENO method is used not only to remove sub-stencils across discontinuities in the reconstruction but also to select flux as a detector as shown in the following equation:

$$F_{i+1/2}^{\mathbf{Riemann}}(u_{i+1/2}^{L}, u_{i+1/2}^{R}) = \begin{cases} F_{i+1/2}^{\mathbf{low}}(u_{i+1/2}^{L}, u_{i+1/2}^{R}), & \text{if } \delta_{3}^{L} \text{ and } \delta_{3}^{R}, \\ F_{i+1/2}^{\mathbf{high}}(u_{i+1/2}^{L}, u_{i+1/2}^{R}), & \text{otherwise.} \end{cases}$$
(7.1)

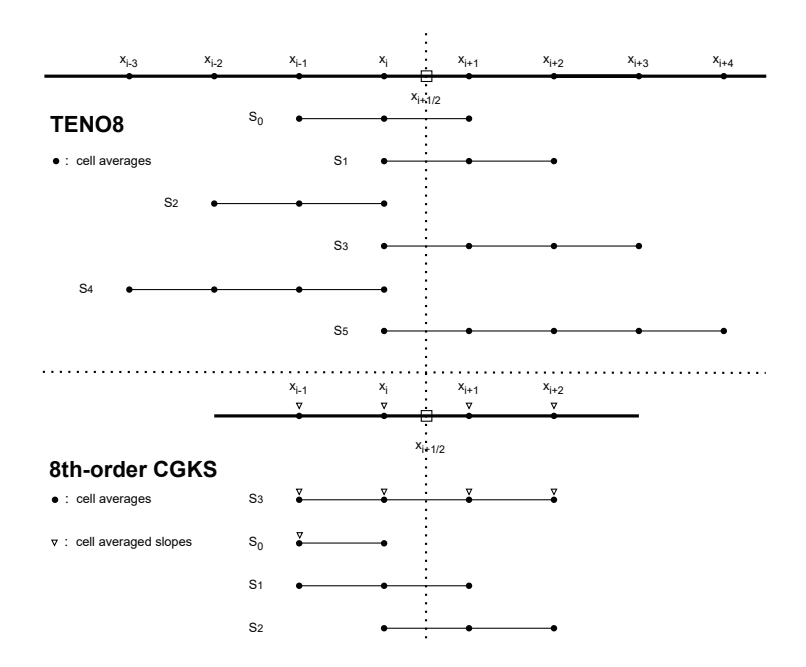


Figure 17: Sub-stencils in the reconstruction for left side value of the interface  $x_{i+1/2}$  in the TENO8 and CGKS 8th-order reconstruction: the circles represent cell averages and the gradients represent cell average slopes.

The reason for the low dissipation in the TENO method is that smooth stencils use a large five-point stencil with a non-dissipative central flux, and non-smooth stencils use a nonlinear reconstruction between three small stencils with a dissipative Riemann flux, e.g., HLLC [7]. However, the performance of the TENO reconstruction only depends on the reconstructed left and right values at the interface at the beginning of the time step. The dissipation for the non-smooth region will depend on the selected Riemann solver flux. As a reconstruction method, TENO is unrelated to the gas evolution process in the timestep.

On the other hand, the flux evaluation in GKS is based on the time evolution of the solution in the kinetic model for a physical process from the initial non-equilibrium state towards an equilibrium one. In the smooth region, GKS can accurately recover the Euler or Navier-Stokes solution. In the discontinuity region, the particle-free transport mechanism introduces numerical dissipation within a shock layer and stabilizes the numerical shock structure. The non-equilibrium state and equilibrium state retain the local spatial variations, which are lost in the traditional Riemann solvers.

Furthermore, the GKS flux solver requires the use of point values and derivatives of both non-equilibrium and equilibrium states at the cell interface. In the spatial reconstruction process, both WENO5-GKS and TENO5-GKS reconstruct the equilibrium and non-equilibrium parts separately. However, unlike the traditional Riemann solver, the time-dependent gas distribution function in GKS at a cell interface provides not only the

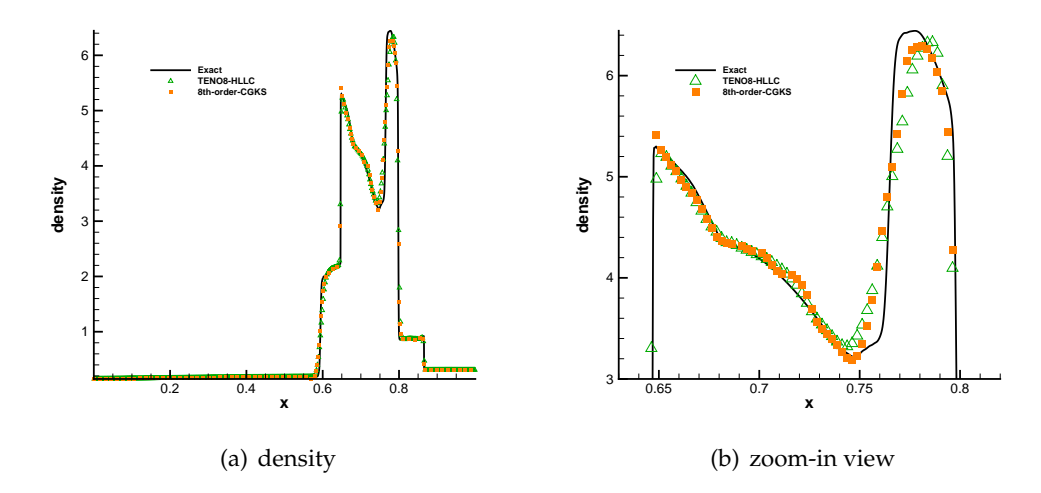


Figure 18: The density distributions for blast wave problem from TENO8-HLLC and 8th-order compact GKS.  $t\!=\!0.038$  and 200 mesh points,  $CFL\!=\!0.5$ .

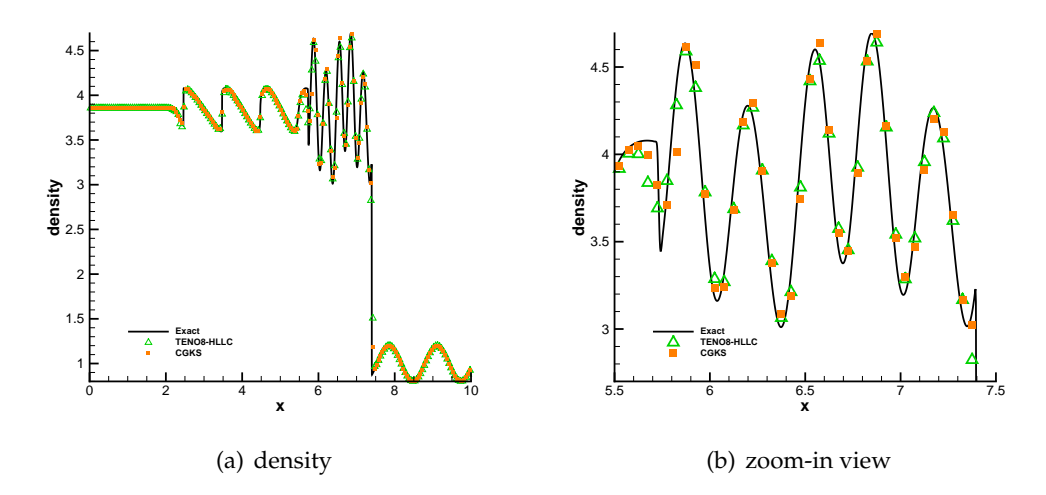


Figure 19: The density distributions for Shu-Osher problem. The results were obtained by 8th-order compact GKS and TENO8-HLLC at  $t\!=\!1.8$  with 200 mesh points.

flux and its time derivative but also time-accurate flow variables at the cell interface. By using the updated cell interface value, slopes of flow variables inside each control volume can be obtained and high-order compact GKS can be constructed [13].

In Fig. 18 and Fig. 19, we compared TENO8-HLLC with 8th-order compact GKS (CGKS) for the Shu-Osher problem. CGKS shows better results than TENO8-HLLC. This comparison indicates that the dynamics of the 1st-order Riemann solver are not enough for the construction of higher-order schemes. Because the physical propagation speed is

limited as we transition from kinetic particle transport to hydrodynamic wave propagation [35], the fluid element is dynamically connected only to its neighboring elements. The CFL number serves not only to determine the time step but also to quantify the relative physical domain for the numerical domain.

In ideal cases, the numerical domain of dependence for any scheme should be the same as the physical domain of dependence. In contrast, for the current existing schemes, there may be a large disparity between them. This disparity is due to the inconsistency between the first-order Riemann solver and the higher-order dynamics requirement in the higher-order schemes. To compensate for the physical weakness in the 1st-order Riemann solver, a strategy like TENO reconstruction may be used to obtain a more reliable and accurate value at the cell interface. However, with the implementation of high-order gas evolution models, such as GRP and GKS, both the numerical and physical domains of dependence are approaching each other in the corresponding higher-order compact schemes. Fig. 18 and Fig. 19 show the ability of CGKS in maintaining high-order accuracy and robustness. Fig. 17 shows the sub-stencils in the reconstruction for the left side value of the interface  $x_{i+1/2}$  in the TENO8 and CGKS 8th-order reconstruction. To achieve the same order, CGKS can use a smaller spatial size of sub-stencils in the compact schemes compared to the TENO8 with a traditional Riemann solver. This merit makes the CGKS more flexible in porting to an unstructured mesh as it uses less cell stencil.

# 8 Summary and conclusions

A performance comparison for high-order schemes, namely, WENO5-GKS, WENO5-HLLC, WENO5-LF, TENO5-GKS, TENO5-HLLC, TENO5-LF, is presented in this paper. TENO5-LF and TENO5-HLLC, as two TENO class Riemann solvers, are compared with the previous two WENO class solvers, WENO5-LF and WENO5-HLLC. In the TENO reconstruction, due to its stencil selection similar to ENO, TENO can control the dissipation of smooth and non-smooth regions. Different from traditional WENO schemes, which lead to smoother stencils by convex combination, the TENO scheme functions as a discontinuity sensor by suppressing the stencils that are detected as non-smoothness stencils based on a predetermined threshold. TENO shows a great improvement in resolving high-frequency problems like the Toro problem and shows its ability to treat discontinuities in the two-dimensional Riemann problem. In the one-dimensional case Toro problem, TENO5-GKS shows better accuracy in smooth regions. In two-dimensional problems, TENO-GKS can capture more vortex structure than WENO-GKS, WENO-LF, and TENO-LF.

On the other hand, TENO reconstruction breaks the symmetry of the flow in twodimensional problems, such as the interaction of planar shocks, because its accumulated floating-point truncation errors may not be quickly dissipated by numerical viscosity. And for the extreme problems with strong pressure jump such as the Noh problem, lowdissipative TENO reconstruction diverges in the early stage. As noted in Section 3, the numerical dissipation comes from  $|\tilde{\partial}_{i+1/2}|(u_{i+1/2}^R - u_{i+1/2}^L)$ . The high-order TENO scheme can detect the non-smooth stencil with the scale separation strategy, a dissipative Riemann solver is still needed to handle the non-smooth scales, i.e., the dissipation of the scheme will depend on the choice of the Riemann solver. By comparing different choices of the Riemann solver, GKS presents favorable robustness in the Noh problem. For three-dimensional Taylor-Green Vortex, WENO5-GKS and TENO5-GKS can take a larger time step with CFL number 0.5, instead of 0.3 for WENO5-HLLC. Meanwhile, WENO5-HLLC (TENO5-HLLC) is 56% (57%) more expensive than WENO5-GKS (TENO5-GKS). It shows that GKS can have a slightly better overall efficiency in 3D cases.

In summary, the numerical flux formulation is more critical for a high-order spatial-temporal scheme when simulating physical processes with strong nonlinearity. Choosing a better flux formulation (such as GKS) appears to be more important than choosing a better spatial reconstruction method when balancing the accuracy in resolving small-scale waves and the robustness in treating strong discontinuities.

# Acknowledgments

This work has been supported by the National Natural Science Foundation of China (NSFC award numbers Nos. T2250710183, U2241269, 11988102), Guangdong Provincial Key Laboratory of Turbulence Research and Applications (2023B1212060001), Guangdong-Hong Kong-Macao Joint Laboratory for Data-Driven Fluid Mechanics and Engineering Applications (No. 2020B1212030001), and Shenzhen Science and Technology Program (No. JCYJ20220530113005012). Computing resources are provided by the Center for Computational Science and Engineering of Southern University of Science and Technology.

#### References

- [1] Dinshaw S Balsara, Sudip Garain, and Chi-Wang Shu, An efficient class of WENO schemes with adaptive order, J. Comput. Phys., 326 (2016), 780–804.
- [2] Prabhu Lal Bhatnagar, Eugene P Gross, and Max Krook, A model for collision processes in gases. I. Small amplitude processes in charged and neutral one-component systems, Phys. Rev., 94(3) (1954), 511.
- [3] Rafael Borges, Monique Carmona, Bruno Costa, and Wai Sun Don, An improved weighted essentially non-oscillatory scheme for hyperbolic conservation laws, J. Comput. Phys., 227(6) (2008), 3191–3211.
- [4] Rafael Borges, Monique Carmona, Bruno Costa, and Wai Sun Don, An improved weighted essentially non-oscillatory scheme for hyperbolic conservation laws, J. Comput. Phys., 227(6) (2008), 3191–3211.
- [5] James DeBonis, Solutions of the Taylor-Green vortex problem using high-resolution explicit finite difference methods, In 51st AIAA Aerospace Sciences Meeting Including the New Horizons Forum and Aerospace Exposition, page 382, 2013.

- [6] Nico Fleischmann, Stefan Adami, and Nikolaus A Adams, Numerical symmetry-preserving techniques for low-dissipation shock-capturing schemes, Comput. Fluids, 189 (2019), 94–107.
- [7] Lin Fu, A low-dissipation finite-volume method based on a new teno shock-capturing scheme, Comput. Phys. Commun., 235 (2019), 25–39.
- [8] Lin Fu, Xiangyu Y Hu, and Nikolaus A Adams, A family of high-order targeted ENO schemes for compressible-fluid simulations, J. Comput. Phys., 305 (2016), 333–359.
- [9] Lin Fu, XY Hu, and Nikolaus A Adams, A targeted ENO scheme as implicit model for turbulent and genuine subgrid scales, Commun. Comput. Phys., 26(2) (2019), 311–345.
- [10] Ory Haimovich and Steven H Frankel, Numerical simulations of compressible multicomponent and multiphase flow using a high-order targeted ENO (TENO) finite-volume method, Comput. Fluids, 146 (2017), 105–116.
- [11] Ami Harten, Stanley Osher, Björn Engquist, and Sukumar R Chakravarthy, Some results on uniformly high-order accurate essentially nonoscillatory schemes, Appl. Numer. Math., 2(3-5) (1986), 347–377.
- [12] Antony Jameson, Wolfgang Schmidt, and Eli Turkel, Numerical solution of the Euler equations by finite volume methods using Runge Kutta time stepping schemes, In 14th Fluid and Plasma Dynamics Conference, page 1259, 1981.
- [13] Xing Ji, Wei Shyy, and Kun Xu, A gradient compression-based compact high-order gas-kinetic scheme on 3D hybrid unstructured meshes, Int. J. Comput. Fluid Dyn., 35(7) (2021), 485–509.
- [14] Xing Ji and Kun Xu, Performance enhancement for high-order gas-kinetic scheme based on WENO-adaptive-order reconstruction, Commun. Comput. Phys. , 28(2) (2020), 539–590.
- [15] Xing Ji, Fengxiang Zhao, Wei Shyy, and Kun Xu, A family of high-order gas-kinetic schemes and its comparison with Riemann solver based high-order methods, J. Comput. Phys., 356 (2018), 150–173.
- [16] Guang-Shan Jiang and Chi-Wang Shu, Efficient implementation of weighted ENO schemes, J. Comput. Phys., 126(1) (1996), 202–228.
- [17] Peter D Lax and Xu-Dong Liu, Solution of two-dimensional Riemann problems of gas dynamics by positive schemes, SIAM J. Sci. Comput., 19(2) (1998), 319–340.
- [18] Randall J LeVeque and Randall J Leveque, Numerical Methods for Conservation Laws, volume 214. Springer, 1992.
- [19] Jiequan Li and Zhifang Du, A two-stage fourth order time-accurate discretization for Lax–Wendroff type flow solvers I. Hyperbolic Conservation Laws, SIAM J. Sci. Comput., 38(5) (2016), A3046–A3069.
- [20] Meng-Sing Liou and Christopher J Steffen Jr, A new flux splitting scheme, J. Comput. Phys., 107(1) (1993), 23–39.
- [21] Xu-Dong Liu, Stanley Osher, and Tony Chan, et al., Weighted essentially non-oscillatory schemes, J. Comput. Phys., 115(1) (1994), 200–212.
- [22] William F Noh, Errors for calculations of strong shocks using an artificial viscosity and an artificial heat flux, J. Comput. Phys., 72(1) (1987), 78–120.
- [23] Liang Pan and Kun Xu, High-order gas-kinetic scheme with three-dimensional WENO reconstruction for the Euler and Navier-Stokes solutions, Comput. Fluids, 198 (2020), 104401.
- [24] Liang Pan, Kun Xu, Qibing Li, and Jiequan Li, An efficient and accurate two-stage fourth-order gas-kinetic scheme for the Euler and Navier–Stokes equations, J. Comput. Phys., 326 (2016), 197–221.
- [25] Philip L Roe, Approximate Riemann solvers, parameter vectors, and difference schemes, J.

- Comput. Phys., 43(2) (1981), 357–372.
- [26] Vladimir A Titarev and Eleuterio F Toro, ADER: Arbitrary high order Godunov approach, J. Sci. Comput., 17 (2002), 609–618.
- [27] Vladimir A Titarev and Eleuterio F Toro, Finite-volume WENO schemes for three-dimensional conservation laws, J. Comput. Phys., 201(1) (2004), 238–260.
- [28] Titarev, Vladimir A and Toro, Eleuterio F, ADER schemes for three-dimensional non-linear hyperbolic systems, J. Comput. Phys., 204(2) (2005), 715–736.
- [29] Eleuterio F Toro, Riemann Solvers and Numerical Methods for Fluid Dynamics: a Practical Introduction, Springer Science & Business Media, 2013.
- [30] Eleuterio F Toro, Michael Spruce, and William Speares, Restoration of the contact surface in the HLL-Riemann solver. Shock Waves, 4(1) (1994), 25–34.
- [31] Wim M Van Rees, Anthony Leonard, Dale I Pullin, and Petros Koumoutsakos, A comparison of vortex and pseudo-spectral methods for the simulation of periodic vortical flows at high reynolds numbers, J. Comput. Phys., 230(8) (2011), 2794–2805.
- [32] Hiro Wakimura, Shinichi Takagi, and Feng Xiao, Symmetry-preserving enforcement of low-dissipation method based on boundary variation diminishing principle, Comput. Fluids, 233 (2022), 105227.
- [33] Paul Woodward and Phillip Colella, The numerical simulation of two-dimensional fluid flow with strong shocks, J. Comput. Phys., 54(1) (1984), 115–173.
- [34] Kun Xu, A gas-kinetic BGK scheme for the Navier–Stokes equations and its connection with artificial dissipation and Godunov method, J. Comput. Phys., 171(1) (2001), 289–335.
- [35] Kun Xu and Chang Liu, A paradigm for modeling and computation of gas dynamics, Phys. Fluids, 29(2) (2017), 026101.
- [36] Kun Xu, Meiliang Mao, and Lei Tang, A multidimensional gas-kinetic BGK scheme for hypersonic viscous flow, J. Comput. Phys., 203(2) (2005), 405–421.
- [37] Xiaojian Yang, Xing Ji, Wei Shyy, and Kun Xu, Comparison of the performance of high-order schemes based on the gas-kinetic and HLLC fluxes, J. Comput. Phys., 448 (2022), 110706.
- [38] Jun Zhu and Chi-Wang Shu, A new type of multi-resolution WENO schemes with increasingly higher order of accuracy, J. Comput. Phys., 375 (2018), 659–683.